J. Fluid Mech. (2012), *vol.* 711, *pp.* 437–468.
doi:10.1017/jfm.2012.400

Direct numerical simulation of a spatially developing compressible plane mixing layer: flow structures and mean flow properties

Qiang Zhou, Feng He† and M. Y. Shen

Department of Engineering Mechanics, School of Aerospace, Tsinghua University, Beijing 100084, PR China

(Received 13 January 2012; revised 28 July 2012; accepted 3 August 2012; first published online 28 September 2012)

The spatially developing compressible plane mixing layer with a convective Mach number of 0.7 is investigated by direct numerical simulation. A pair of equal and opposite oblique instability waves is introduced to perturb the mixing layer at the inlet. The full evolution process of instability, including formation of Λ-vortices and hairpin vortices, breakdown of large structures and establishment of self-similar turbulence, is presented clearly in the simulation. In the transition process, the flow fields are populated sequentially by Λ-vortices, hairpin vortices and 'flower' structures. This is the first direct evidence showing the dominance of these structures in the spatially developing mixing layer. Hairpin vortices are found to play an important role in the breakdown of the flow. The legs of hairpin vortices first evolve into sheaths with intense vorticity then break up into small slender vortices. The later flower structures are produced by the instability of the heads of the hairpin vortices. They prevail for a long distance in the mixing layer until the flow starts to settle down into its self-similar state. The preponderance of slender inclined streamwise vortices is observed in the transversal middle zone of the transition region after the breakup of the hairpin legs. This predominance of streamwise vortices also persists in the self-similar turbulent region, though the vortices there are found to be relatively very weak. The evolution of both the mean streamwise velocity profile and the Reynolds stresses is found to have close connection to the behaviour of the large vortex structures. High growth rates of the momentum and vorticity thicknesses are observed in the transition region of the flow. The growth rates in the self-similar turbulence region decay to a value that agrees well with previous experimental and numerical studies. Shocklets occur in the simulation, and their formation mechanisms are elaborated and categorized. This is the first three-dimensional simulation that captures shocklets at this low convective Mach number.

Key words: compressible turbulence, free shear layers, transition to turbulence

1. Introduction

Recently, the renewed interest in scramjets (supersonic combustion ramjets) has led to extensive numerical and experimental investigations on the compressible shear layer. The main restriction of the scramjet technique is the reduced growth rate of the

† Email address for correspondence: hefeng@tsinghua.edu.cn

mixing between fuel and oxidizer, which is still poorly understood. The work on the compressible mixing layer will also benefit high-speed civil transport regarding noise reduction (Moore 1978).

The first investigation of the mixing layer was performed by Liepmann & Laufer (1947), demonstrating that the flow is self-preserving. Self-preservation is an important property of the mixing layer. It implies that 'a moving equilibrium is set up in which conditions at the initiation of the flow are highly irrelevant' (Townsend 1976, p. 196). This property puts a limit on the influencing region of mixing enhancing methods adopted upstream. Therefore, the present paper will not focus on pursuing a forcing strategy that can increase the growth rate in the self-similar region. Instead, we aim to understand in detail the typical evolution of the vortical structures in the compressible mixing layer under the forcing of linearly unstable disturbances. The idea of thickening the mixing layer before it evolves into the self-similar state will also be examined.

Large quasi-two-dimensional coherent vortical structures in subsonic turbulent free shear flows were first observed by Brown & Roshko (1974) experimentally, which highlighted the significance of larger structures and markedly altered perceptions of these flows. Ortwerth & Shine (1977) provided early experimental evidence that large-scale structures exist in supersonic shear layers though they did not explore the structures in detail. Bogdanoff (1983) and Papamoschou & Roshko (1988) first used the concept of convective Mach number, M_c, to quantify the compressibility in the compressible shear layer, which is based on the velocity difference between the convection of the structures and the external flow. Through a series of experiments, Clemens & Mungal (1992, 1995) found that, as convective Mach number increases, the mixing layer becomes highly three-dimensional, with little apparent two-dimensional large-scale organization. They claimed that this change was due to the compressibility effect and was not a Reynolds number effect. Rossmann, Mungal & Hanson (2002) observed that thin streamwise vortical structures dominated the flow topology at the convective Mach number of 1.7. Recently, Watanabe & Mungal (2005) reported that a pair of stationary counter-rotating streamwise vortices was prevalent even in the fully developed region of the shear layers.

Through linear stability analysis, Sandham & Reynolds (1990) revealed that three-dimensional modes are dominant in the high-speed mixing layer above a convective Mach number of 0.6. The linear theory can be very useful for investigating the physics of free shear layers because it has been demonstrated by Sandham & Reynolds (1991) that simulations with purely random initial conditions give a structure very similar to the structures developing from the linearly most unstable pair of equal and opposite oblique waves obtained from the liner theory. Since then, instability waves have been used to disturb the initial flow in temporal developing simulations by many researchers (e.g. Vreman, Kuerten & Geurts 1995; Fu, Ma & Zhang 2000; Kourta & Sauvage 2002). In our spatially developing simulation, the linearly most unstable waves are also used at the inlet to perturb the flow periodically since they can facilitate our simulation without changing the basic physics.

Thanks to the recent advancements in high-order-accuracy schemes, high-speed computers and interactive graphics tools over the past two decades, direct numerical simulation (DNS) of the compressible temporal developing mixing layer has become affordable. Most probably, Sandham & Reynolds (1991) were the first researchers who identified the inclined Λ-vortex in the temporal simulations at $M_c = 0.8$. Vreman *et al.* (1995) and Kourta & Sauvage (2002) also observed inclined Λ-vortices at $M_c = 1.2$ in their numerical investigations. Fu *et al.* (2000) presented the whole evolution process

of the mixing layer at $M_c = 0.8$. They found that the development goes from formation of Λ-vortices, through double horseshoe vortices and mushroom structures to the final turbulent state with smaller vortices. They stressed that there is not the vortex pairing in the transition process which usually happens in incompressible shear flows. In comparison with the temporally developing flow, DNS of the spatially developing flow is more computationally demanding. Recently, Fu & Li (2006) performed a simulation of a spatially developing mixing layer and reported that oblique structures are more prevalent in the flow with higher M_c. However, they also mentioned that their computational mesh might not be fine enough to reveal the structure evolution more closely since the residual of the Reynolds stress transport balance was not adequately small in their simulations. One of the objectives of the present paper is to illustrate the detailed development process of the vortical structures in the compressible mixing layer. The more physically sound spatial frame for simulation is adopted. The grid spacing is checked in several ways to make sure our results are of physical not numerical origin.

Distortion of the mean streamwise velocity profile was observed by many experimental investigators. To the best of our knowledge, Nygaard & Glezer (1991) first reported an S-shaped velocity profile in the incompressible mixing layer. They pointed out that this phenomenon was accompanied by the onset of streamwise vortices. Later on, Foss & Zaman (1999) observed similar phenomenon in their study of the incompressible flow perturbed by tabs. More recently, a profile with triple inflections was observed by Watanabe & Mungal (2005) in a forced compressible mixing layer of $M_c = 0.62$. They remarked that multiple inflection points appeared to enhance shear-layer instability, leading to a mixing enhancement. Though the distortion of the streamwise velocity profile has been observed many times, the reason behind it has not been deeply explored. In our numerical work, this phenomenon occurs and is understood with the help of vortical visualization.

It is well-recognized that the transversal Reynolds stress and the Reynolds shear stress decrease as the convective Mach number increases. This was first observed experimentally by Elliott & Samimy (1990), and later on by Goebel & Dutton (1991), Gruber, Messersmith & Dutton (1993), Urban & Mungal (2001) and Olsen & Dutton (2003). However, there are some controversies about the changing trends of the streamwise and the spanwise Reynolds stresses. Elliott & Samimy (1990) stated that all Reynolds stresses decrease significantly as M_c increases while Goebel & Dutton (1991) claimed that the streamwise Reynolds stress only changed slightly. Also, Gruber *et al.* (1993) reported a basically constant spanwise Reynolds stress in their experimental investigation as M_c varied. This controversy also exists in the computational community. Pantano & Sarkar (2002) and Fu & Li (2006) reported the decrease of all Reynolds stress components as M_c increased while Freund, Lele & Moin (2000) observed a constant streamwise Reynolds stress. In this study, the transversal Reynolds stress and the shear stress agree well with previous results. However, a deviation of the streamwise and spanwise Reynolds stresses from experimental results is found. The possible underlying reasons are discussed carefully in this study.

In compressible mixing layers, the occurrence of shocklets has been seen when convective Mach number is higher than 0.7 in two-dimensional simulations (Lele 1989). For three-dimensional simulations, shocklets are also captured when the convective Mach number reaches 1.2 (Vreman *et al.* 1995; Kourta & Sauvage 2002; Fu & Li 2006). The existence of shocks has also been confirmed by powerful visualization and measurement techniques (Papamoschou 1995; Rossmann *et al.* 2002).

In most of the previous work, numerical simulations were done in the temporal frame. This paper will report the occurrence of shocklets in a spatially developing compressible mixing layer of $M_c = 0.7$. The reason why the shocklets are captured at such a low M_c in three-dimensional flow is also addressed.

This paper is structured in the following manner. In § 2, the details of the simulation are presented along with the validation of the results. Then, the visualizations of the large structures are performed in § 3. The mechanism of the transition is also discussed in this section. Section 4 addresses the spatial evolution of the mean streamwise velocity and also pursues a discussion on the growth rate of the compressible mixing layer. Section 5 provides the evolution of the Reynolds stresses. Section 6 presents the occurrence of shocklets. The shocklet formation mechanisms are elucidated with the aid of structure visualizations. Finally, we give concluding remarks in § 7.

2. Computation details

The unsteady, three-dimensional, compressible Navier–Stokes equations are solved for the spatially evolving shear layer. The ideal gas law is used to relate the state variables. The quantities in the high-speed stream (upper stream) and low-speed stream (lower stream) are denoted by variables with subscript 1 and subscript 2, respectively. All variables are non-dimensionalized by the initial vorticity thickness $\delta_{\omega 0}$ and the free-stream parameters of the high-speed stream, such as density ρ_1, velocity U_1, and temperature T_1. The pressure is non-dimensionalized by the product $\rho_1 U_1^2$. The non-dimensional viscosity has a power-law dependence on the non-dimensional temperature: $\mu = T^{0.768}$ (Morduchow & Libby 1949). The Prandtl number is set to 0.75.

The computational domain is defined as $[0, mL_x] \times [-L_y/2, L_y/2] \times [0, nL_z]$, where $L_x = 2\pi/\alpha = 11.58, L_y = 400, L_z = 2\pi/\beta = 17.45$. The α and β correspond to the streamwise and spanwise wavenumber of the most unstable oblique mode from linear stability analysis (Sandham & Reynolds 1990). Our tests show that a surprisingly long streamwise domain is needed to make the flow settle down to the fully developed turbulence. The parameter m is set to 54; and we choose $n = 2$ to ensure that the spanwise extent of the computational box is adequate in the sense that spanwise two-point correlations decay sufficiently close to zero.

The computational domain is bounded by inflow and outflow boundaries in the streamwise x-direction, two non-reflecting boundaries in the normal y-direction (Thompson 1987), and two periodic boundaries in the spanwise z-direction. At the inflow boundary, the unperturbed basic inflow profile is a time-independent laminar compressible-boundary-layer similarity solution (Sandham & Reynolds 1990). The mixing layer is periodically forced by a pair of the linearly most unstable oblique waves of equal amplitudes (the amplitude is 0.2 relative to the mean profile). The forcing frequency ω is 0.41, which is also determined through the linear stability theory. Sandham & Reynolds (1991) have shown that simulations with forcing of linear instability waves produced the development of large-scale structures similar to a fully nonlinear computation with a random initial condition. In addition to oblique waves, vortex disturbances with axis along the y-direction are also introduced at the frequency ω. The vortex disturbances come from an isentropic vortex model (Davoudzadeh, McDonald & Thompson 1995; Jiang & Shu 1996). We denote the vortex disturbances with axis located at (x_c, z_c) by a prime: $u' = \varepsilon\tau \mathrm{e}^{\sigma(1-\tau^2)} \sin\theta$, $w' = -\varepsilon\tau \mathrm{e}^{\sigma(1-\tau^2)} \cos\theta$, $T' = -(\gamma - 1)\varepsilon^2 \mathrm{e}^{2\sigma(1-\tau^2)}/4\sigma\gamma$, where $\varepsilon = 0.05\mathrm{e}^{-y^2}$, $\tau = r/r_c$, and $r = \sqrt{(x - x_c)^2 + (z - z_c)^2}$. The γ in the formula for T' is the specific heat

ratio, which has a value of 1.4. Note that $\varepsilon = 0.05\mathrm{e}^{-y^2}$ controls the strength of the disturbances. The exponential expression indicates that the disturbances decay very fast away from the middle plane (the plane of $y = 0$) of the mixing layer. The decay rate of the vortex is controlled by σ, and r_c is the critical radius at which the disturbances reach maximum strength. In this paper, we choose $\sigma = 0.5$ and $r_c = L_z/16$.

At the inlet, four columns of vortex disturbances enter the computational domain at the speed of ω/α, which is the same as the phase velocity of the linear instability waves. The centres of vortices in the four columns lie on the same z-line. Note that the total kinetic energy content of the vortex disturbances is relatively very weak, only 0.91 % of that of the added linear unstable waves. The introduction of the vortex disturbances is only to break up the symmetry of the flow in the z-direction slightly, which gives the inflow condition some natural asymmetric properties and helps the flow develop into turbulence earlier. In the present simulation, Mach numbers of the upper stream and the lower stream M_1, M_2 are set to 2.8 and 1.4, respectively. Assuming equal specific heats and temperatures, gives $M_c = (M_1 - M_2)/2 = 0.7$. The pressures of both free streams are the same and equal $1/(\gamma M_1^2)$. The Reynolds number Re used in this simulation equals 800.

The finite-difference grid size is $4160 \times 351 \times 256$ along the x-, y- and z-directions, respectively. In the x-direction, the first 4000 grid points are uniformly spaced from $x = 0$ to $x = 50L_x$, while the other 160 grid points are stretched from $x = 50L_x$ to $x = 54L_x$ to make a buffer range. In the normal direction, in order to capture the fine structures in the mixing layer, the grid is concentrated in the middle zone and stretched to the far-field boundaries. In the spanwise direction, the grid is uniformly spaced. Note that we do not perform simulations with difference grid spacings to check the grid independence since this would be prohibitively computationally demanding. The current mesh is indeed fine enough to compute all relevant scales.

We support this claim in the following four ways. First, using the initial vorticity thickness as the characteristic length, the minimum mesh sizes in the x-, y- and z-directions are $\Delta x = 0.145$, $\Delta y = 0.167$ and $\Delta z = 0.136$, respectively. They are slightly smaller than those used in the previous DNS of a temporally developing plane mixing layer (Pantano & Sarkar 2002), in which $\Delta x = \Delta y = \Delta z = 0.167$. Also, the Reynolds number based on the velocity difference of the two sides is 400 in our simulation. It is smaller than the value 640 adopted by Pantano & Sarkar (2002). This difference further indicates that our mesh is finer. Second, the spanwise energy spectrum of the streamwise velocity fluctuation is checked in the fully developed turbulence region. It is shown (see figure 1) that the spectrum yields a significant range with -7 slope in the high-wavenumber range. This result is consistent with the theoretical analysis in the viscous subrange by Heisenberg (1948) and Batchelor (1959), demonstrating that the finest scales in the turbulence have been resolved in the simulation. We do not see an apparent range with $-5/3$ slope in the spectrum, most likely due to the low Reynolds number of the DNS. Third, we show the residual and the turbulent kinetic energy budget in figure 2. It can be seen that the numerical dissipation is small and negligible compared to the physical dissipation, ensuring that the turbulent flow we captured is of physical rather than numerical origin. Fourth, the normalized growth rate of the momentum thickness of the mixing layer is compared with published experimental, numerical and theoretical results (see figure 3). The normalized growth rate is $(\dot{\delta}_\theta/\dot{\delta}_{\theta 0})/((U_1 - U_2)/(U_1 + U_2))$ (see Pantano & Sarkar 2002), where $(U_1 - U_2)/(U_1 + U_2)$ is the velocity ratio, and $\dot{\delta}_\theta$, $\dot{\delta}_{\theta 0}$ denote the momentum thickness growth rate in the present simulation and that of an incompressible mixing layer, respectively. According to Pantano & Sarkar (2002), $\dot{\delta}_{\theta 0}$ is set to 0.032, one

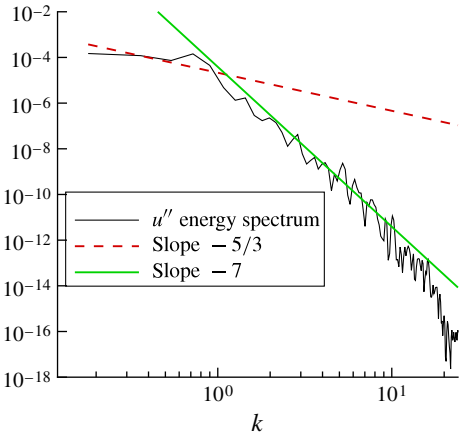

FIGURE 1. (Colour online) The spanwise energy spectrum of the streamwise velocity fluctuation in the self-similar turbulence region, where k is the spanwise wavenumber.

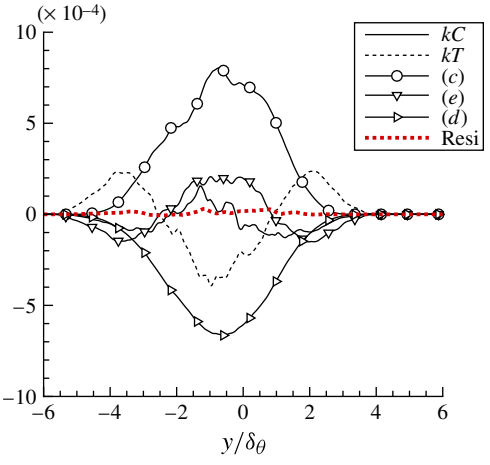

FIGURE 2. (Colour online) The turbulent kinetic energy budget in the self-similar turbulence region, where kC, kT, (c), (e), (d) denote the convective, transport, production, pressure dilatation and dissipation terms respectively. Resi denotes the residual error of the turbulent kinetic energy transport equation. The δ_θ used to normalize y denotes the momentum thickness of the mixing layer, defined $(1/\rho_1 \Delta U^2) \int_{-L_y/2}^{L_y/2} \bar{\rho}(U_1 - \tilde{u})(\tilde{u} - U_2)\,\mathrm{d}y$.

fifth of the corresponding growth rate of the vorticity thickness. The present result fits well with the trend of the scattered experimental results (solid symbols) and the prediction from linear stability analysis by Day & Reynolds (1998). So, we believe the four results stated above have provided solid validation of the DNS results. In addition, we also want to check if the computational domain is wide enough for the turbulence simulation. This is done through the spanwise two-point correlations of pressure and velocity components shown in figure 4, where the data are extracted from a z-line located in the self-similar turbulence region. It can be seen that the correlations decay

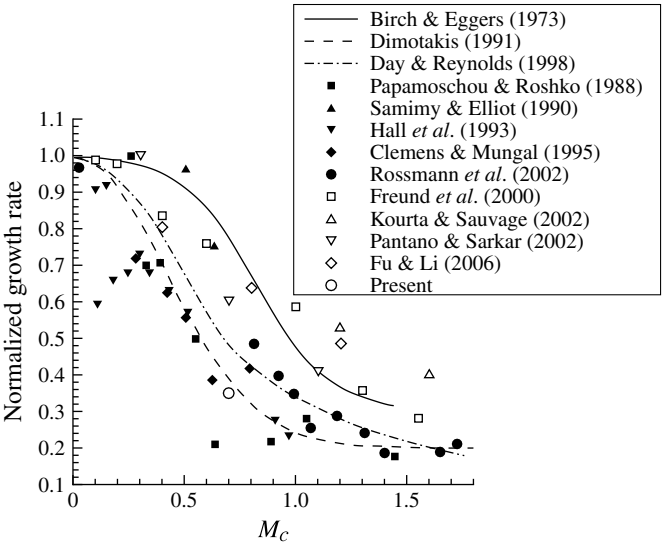

FIGURE 3. Comparison of the growth rate of the mixing layer in the self-similar turbulence state. The curves show results from experimental fitting (Birch & Eggers 1973; Dimotakis 1991) or from a linear stability analysis (Day & Reynolds 1998). The solid symbols denote experimental results, while the open symbols represent numerical results.

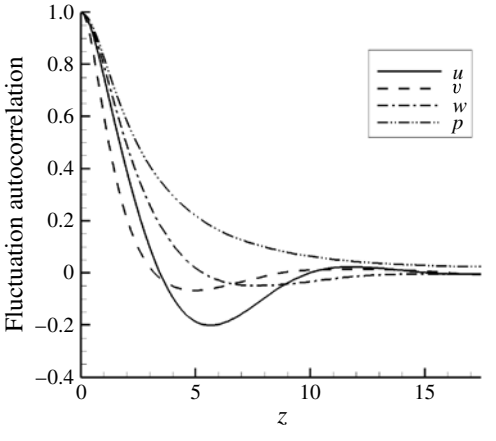

FIGURE 4. The spanwise two-point correlations of pressure and velocity components in the self-similar turbulence region.

sufficiently at the half-width of the computational box, indicating that the spanwise span of the computational box is appropriate for the turbulence simulation.

We adopt finite-difference methods to solve the full Navier–Stokes equations. In the Steger–Warming splitting building block (Steger & Warming 1981), the latest developed high-order high-resolution hybrid scheme 7P7Om2 (Zhou *et al.* 2007) is used for spatial discretization of convective flux terms. The explicit central eighth-order scheme is adopted for viscous flux terms. The time integration is performed by means of an eight-stage, fourth-order, strong-stability-preserving Runge–Kutta scheme

(Spiteri & Ruuth 2003). The simulation is performed using 960 processors on Intel Xeon E5450 nodes. The computational time step is fixed at $\Delta t = 0.125$, which is $\sim 1/120$ of the forcing period T. It took 16 000 time steps to purge the transient flow and establish statistically steady state. Another 28 000 time steps are used to capture sufficient information in order to have unsteady data for statistical analysis. Also, the statistical sample is enhanced by averaging in the spanwise direction. Two types of averages are used in this paper. An overbar, $\bar{u}$, indicates a Reynolds average and a tilde, $\tilde{u}$ indicates a density-weighted or Favre average. Fluctuations from Favre averages are indicated with u''. Fluctuations from Reynolds averages are not defined since they are not used in this paper.

3. Visualizations and discussion on instantaneous structures

It has been demonstrated by Zhou, Adrian & Balachandar (1999) that using the iso-surface of swirl strength is a good method to visualize vortices. Therefore, this paper adopts this method to show the vortex structures in the mixing layer.

Figure 5(*a*) shows the vortex structures in the mixing layer at some instant of time. Iso-surfaces of swirl strength with a value of 0.025 are used. It can be seen that several shear layers appear instantly near the inlet of the mixing layer. These shear layers roll up into Λ-shaped vortices quickly. Λ-vortices then evolve into hairpin vortices. Hairpin vortices are found to play a dominant role in the breakdown of the mixing layer. The legs of hairpin vortices evolve into sheaths with intense vorticity and then break up into small slender vortices. The heads of hairpin vortices experience an instability that leads to previously unreported structures. The new structures consist of many slender vortices and resemble flowers (see the enlarged picture in figure 5*b,c*). We refer to them as flower structures hereafter. The flower structures can sustain themselves over a long distance until the flow reaches self-similar turbulence. In the later turbulence region, the aforementioned large-scale structures disappear completely, whereas plenty of slender small vortices are identified (see the later stages of figure 5*a*).

In addition, it is important to note that the preponderance of hairpin-like structures has recently been reported in a DNS of a spatially developing incompressible boundary layer by Wu & Moin (2009). Both their finding and ours demonstrate the striking significance of hairpin vortices in the breakdown of shear flow transitions.

3.1. *The roll-up of the* Λ*-vortex*

Figure 6(*a*) shows a three-dimensional view of the Λ-vortices near the inlet. We can see that a Λ-vortex is rolled up from the initial high-shear layer at a short distance of around two fundamental streamwise wavelengths. With careful observation, we can also see that there is a small curved shear layer over the junction of the two legs of the Λ-vortex. For convenience, we call the curved shear layer a 'hat' structure since it resembles a hat covering the Λ-vortex. It is conjectured that the vorticity of the hat is the residual vorticity of the main shear layer after the roll-up of the Λ-vortex. The physical connections between the hat and the legs provide clear and convincing evidence for this conjecture. To the best of our knowledge, the hat structure has not been reported in previous studies that identified Λ-vortices (see e.g. Sandham & Reynolds 1991; Fu *et al.* 2000; Kourta & Sauvage 2002). It will be demonstrated later that this structure is the embryonic form of the head of the later hairpin vortex. In addition, we note that the hat on the lower side seems to evolve slightly faster and has

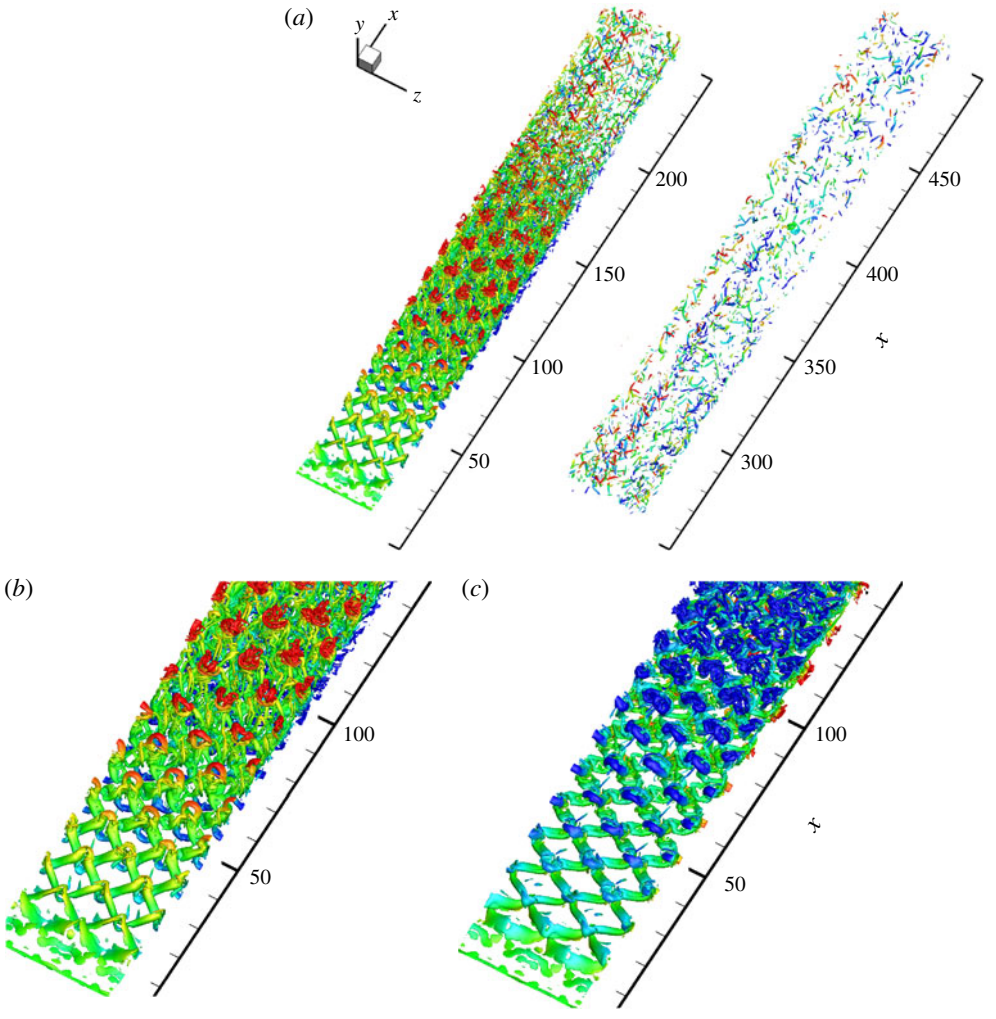

FIGURE 5. (*a*) An instantaneous overall three-dimensional view of the vortex structures in the compressible mixing layer for $M_c = 0.7$. The vortices are shown using the iso-surfaces of swirl strength with a value of 0.025. The colour changes from blue to red as y increases. (*b*) A local enlarged view of (*a*). (*c*) A local enlarged view of the mixing layer from the lower side.

already rolled up to a vortex. This difference of the evolution between the two sides will be discussed below.

Figure 6(*b*) shows the instantaneous field of the spanwise vorticity on the plane through the legs (see figure 6*a*). We can see clearly the roll-up process of the legs, which has been demonstrated before by extensive two-dimensional simulations (e.g. Lele 1989). We can also see that the cross-sections of the legs are evolving rapidly from circular to elliptical due to the strong stretch of the main shear. Though the cross-sections shown in figure 6(*b*) do not belong to one particular leg, every leg in that area changes its shape spatially in that way.

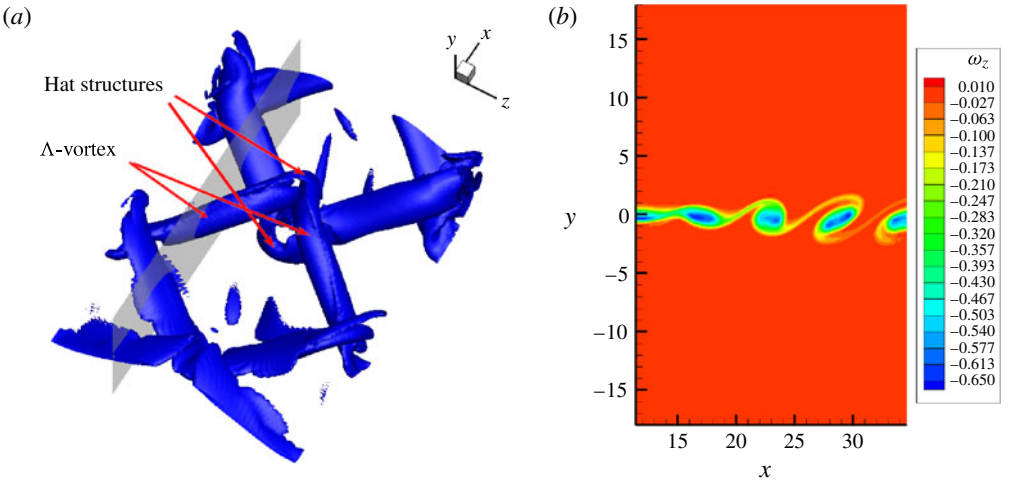

FIGURE 6. (*a*) A three-dimensional view of the Λ-vortices in the streamwise (x) domain [11, 35]. A two-dimensional slice is shown cutting through the legs of several Λ-vortices. (*b*) The instantaneous field of the spanwise vorticity on the slice denoted in (*a*).

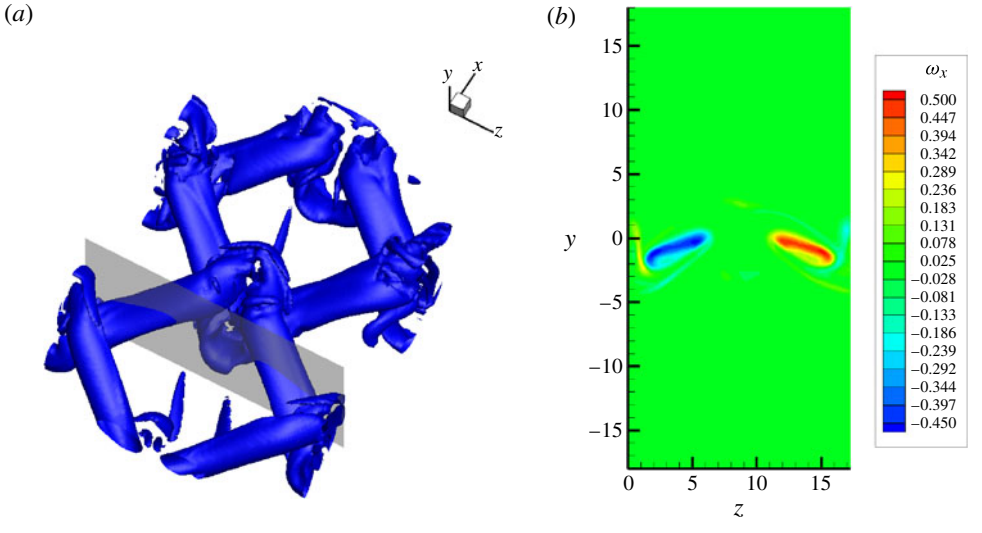

FIGURE 7. (*a*) A three-dimensional view of the Λ-vortices in the streamwise domain [23, 46]. A two-dimensional slice is shown cutting through the legs of a Λ-vortex. (*b*) The instantaneous field of the streamwise vorticity on the slice denoted in (*a*).

The hat in the upper layer also rolled up at a slightly farther distance, as we can see in figure 7(*a*). The legs of the Λ-vortices are all in an elliptical shape at this distance. The streamwise vorticity field on a two-dimensional slice that cuts through the legs of a Λ-vortex is shown in figure 7(*b*), from which we can see the streamwise vorticity is distributed almost uniformly in the flattened legs.

3.2. *The rise of the hairpin vortex and the formation of the sheath structure*

The instantaneous vortex structures in the streamwise domain [46, 70] are shown in figure 8(*a*). We can see that the head vortex has risen up high, indicating that a hairpin vortex has formed. The instantaneous field of the spanwise vorticity on a two-dimensional slice indicated in figure 8(*a*) is given in figure 8(*b*), from which we can see that both the upper and the lower heads have strong concentrated negative spanwise vorticity. The head vortex now looks like an inverted 'U' shape. For clarity of description here, only the top part consisting primarily of spanwise vorticity will be referred to as a hairpin head hereafter. The arms of the 'U' that connect the head and the legs will be referred to as necks of the hairpin vortex (note that in the paper by Zhou *et al.* 1999, necks denote only the small parts of kinks connecting the head and the legs). Apparently, the necks are a pair of counter-rotating normal vortices. Their rotation directions are consistent with that of the head since they belong to the same vortex tube.

The legs of the hairpin vortices develop from the legs of the Λ-vortex. As the flow goes downstream, the head and necks lift up rapidly under the action of mutual induction of the necks while the legs stay almost stationary in the middle of the mixing layer. At this distance, the legs cannot sustain themselves and start to produce small vortices in two ways. On one hand, the kinks between the necks and the legs become unstable and produce smaller vortices. This instability comes from the difference in rotation of the necks and the legs. On the other hand, the legs themselves start to break up. Figure 8(*c*) shows a plane cutting through the legs and figure 8(*d*) gives the field of the streamwise vorticity on this plane. We can see that almost all the vorticity has approached the peripheries of the legs, leaving a low-enstrophy bubble in each leg. We can also see that the legs expand slightly as they become flattened (compare figure 8*d* to figure 7*b*). The entire process of this evolution can be explained well by the theory of the core dynamic instability (CDI) proposed by Schoppa, Hussain & Metcalfe (1995). They found that the expansion of a vortex produces a meridional flow inside it. The meridional flow then moves the vorticity spatially from the vortex centre to the core periphery, leaving the vortex as a thin sheath with intense vorticity. The CDI theory predicts that the sheath would break up finally. However, the breakup in this study does not completely follow the ideal view described by Pradeep & Hussain (2000). They thought the sheaths might undergo Kelvin–Helmholtz (K–H) instability and yield many smaller vortices near peripheries with their axes perpendicular to that of the original sheaths. In figure 8(*c*), it can be seen that the sheaths seem to split mainly into two slender parts in addition to some other smaller parts. The differences in the breakup of the sheaths may be due to the flattened shape and also the low Reynolds number of the current simulation. Nevertheless, the breakup of leg vortices initiates the transition to the shear-flow turbulence.

One of the important consequences of the breakup of the legs is that the connection between the upper layer and the lower layer is lost. This phenomenon can be observed clearly from the side view of the global structure shown in figure 9 at the distance beyond $x = 50$. After the disconnection, the number of hairpin vortices in the lower layer becomes slightly greater than that in the upper layer, indicating that the structures are more compact in the lower layer. The disconnection actually breaks point reflection symmetries between the two sides. It should be noted that the loss of symmetries cannot be captured by the simulation in a temporal frame because several plane and point reflection symmetries would be preserved by the Navier–Stokes equations when simple linear unstable modes are used as initial perturbations (Rogers

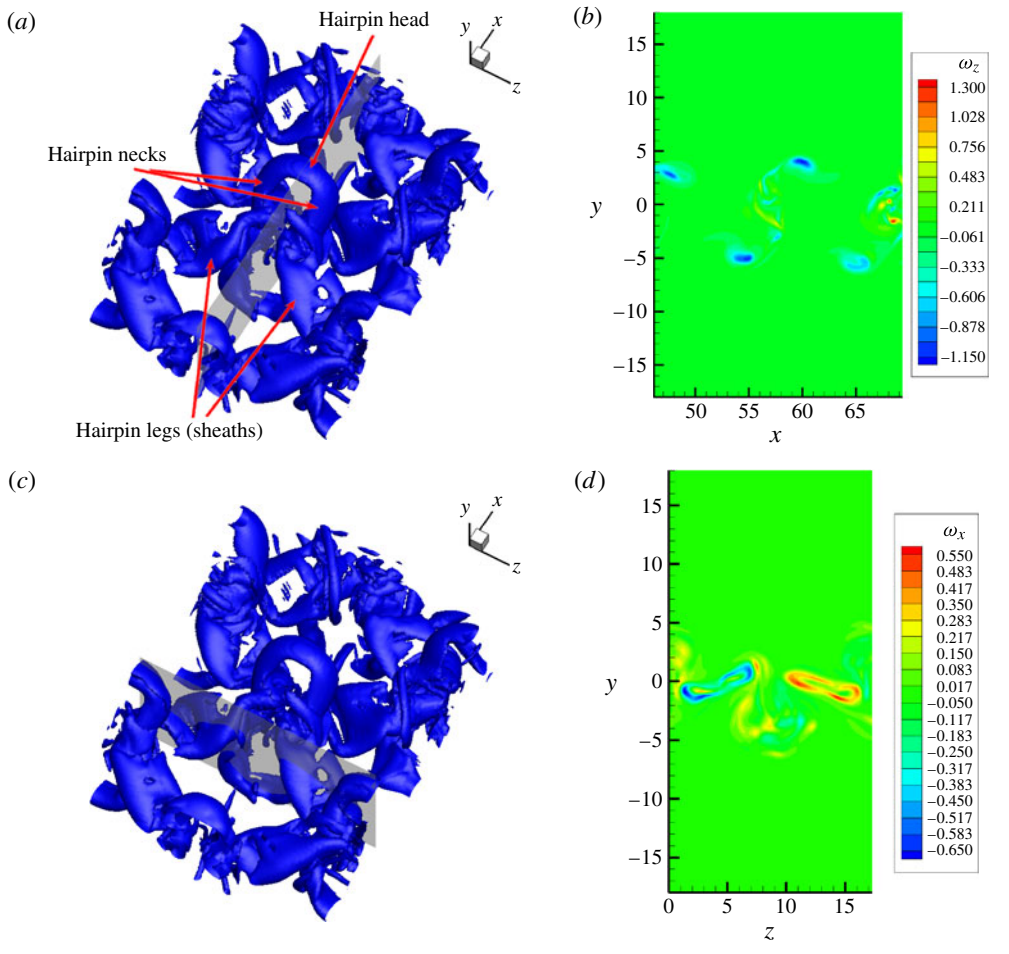

FIGURE 8. (*a*) The structure of a hairpin vortex in the streamwise domain [46, 70]. A two-dimensional slice is shown cutting through the middle of the head of the hairpin vortex. (*b*) The instantaneous field of the spanwise vorticity on the slice denoted in (*a*). (*c*) A two-dimensional slice is shown cutting through the legs of the hairpin vortex. (*d*) The instantaneous field of the streamwise vorticity on the slice denoted in (*c*).

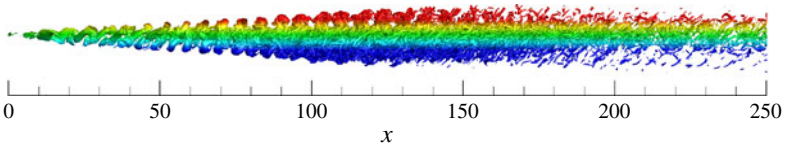

FIGURE 9. The side view of the global structure in the transition region. The relative compactness of the protruded structures is noticeable in the lower layer after the breakup of the inclined leg vortices at around $x = 50$. The colour changes from blue to red as y increases. More vortices in blue are shown downstream, indicating the flow slightly deviates towards the low-speed side (the lower layer).

& Moser 1992; Moser & Rogers 1993). These symmetries can be observed even in the simulation results for a convective Mach number as high as 1.2 (Vreman *et al.* 1995). However, of course, laboratory mixing layers do not possess these symmetries, which strongly suggests that a study on the time-dependent dynamics of the shear flow in the spatial frame will be more physically sound and valuable.

From figure 9, we can see that, after the breakup of the legs, the hairpin vortices on either side are starting to protrude into the free-stream flow on their side. These two sets of hairpin vortices are separated by the small vortices in the middle zone of the mixing layer. This phenomenon is different from that in an incompressible or low compressible flow, where only one set of spanwise rollers resides at the middle of the flow. Once the flow structures approach closer to the free-stream flow, their transport speeds are influenced by the free-stream velocity on their side. The upper set of flow structures will move faster than the lower set. Owing to this difference of transport speeds, the interval between two adjacent structures in the lower layer becomes smaller than that in the upper layer, indicating that the lower layer has more structures in certain streamwise intervals. The larger number of structures on the lower sides would be entraining more fluid as the flow goes downstream, considering the flow structures on either side basically have the same ability to entrain flow from the free stream. This explains the commonly recognized phenomenon that the mixing layer deviates towards the side with lower speed. We can also see that the seemingly faster evolution of the structures in the lower layer is mainly due to the slightly smaller transport speed of the structures. Now the issue raised above that the hat of the Λ-vortex evolves faster than that in the upper layer (see figure 6*a*) can be readily understood. In fact, experimentalists have earlier noticed the asymmetry property in mixing layers of moderate and high convective Mach number through different methods of measurement (see e.g. Papamoschou 1989; Clemens & Mungal 1995). It is noteworthy that Clemens & Mungal (1995) observed reduced magnitude of the mixture-fraction fluctuation especially on the high-speed side of the layer as M_c increases from 0.24 to 0.62 and 0.79. Here, in our case of $M_c = 0.7$, the relatively sparse structures on the high-speed side are consistent with this observation.

3.3. *The formation of the necklace vortex and the instability of the hairpin head*

Figure 10(*a*) shows the vortex structures of the mixing layer in the streamwise domain [69, 93]. In this figure, vortices of positive spanwise vorticity are rendered in red while those of negative spanwise vorticity are rendered in blue. It can be seen that many slender vortices have been produced in the transversal middle zone of the mixing layer after the breakup of the legs. Specially, a semi-ring vortex develops just upstream of the necks. The instantaneous field of spanwise vorticity on a slice cutting through the head is displayed in figure 10(*b*) (the position of the slice is shown in figure 10*a*). It can be seen that two very small red points with strikingly strong positive vorticity appear just upstream of the head, indicating that there are actually two semi-ring vortices. They are very close to each other, making only one clearly identifiable from figure 10(*a*). Close examination shows that these semi-ring vortices originate from the K–H instability of the shear layer produced by the main flow and the pump flow of the hairpin necks. This phenomena may be very common since there exist many strong vortices that could produce mini-shear layers with surrounding flows in the transition region. The semi-ring vortices are referred to as necklaces in this paper because they are around the hairpin necks (see figure 5*b* for a global view).

Here, another question arises: why do the necklaces have a middle segment curved towards upstream, not downstream? It is believed that the orientation of the necklaces

is a consequence of the competition between the hairpin vortices of the upper and the lower layers. As pointed out earlier, the evolution in the lower layer proceeds slightly faster. Therefore, at this distance, the pump flow induced by the upper hairpin necks is more energetic since the hairpin structure in the lower layer has already lost stability and is about to break down. The upper pump flow moves both upstream and upwards against the main flow. It bends the necklaces upstream while lifting them up. Actually, once the middle of the necklace starts to protrude upstream, the necklace itself also induces the entire body to move upwards. Generally, the necklaces are the collaborative products of the hairpin structures on both sides but lifted upwards by the strong pump flow of the upper side. This also explains why necklaces are rarely observed in the lower layer of the flow (see figure 5*c*).

From figure 10(*a*), we can also see that the middle segment of the upper head starts to bend upstream. This is because both the necklaces and the necks induce the middle segment of the head to move upstream. This induction is strong enough to dominate over the main flow that tries to push the middle segment of the head downstream. Once the middle segment of the head moves upstream, even very slightly, the movement will proceed further rapidly. This is because even stronger induction can be felt by the head in the new position. The further bending of the middle segment stretches the head into two almost parallel slender vortices, which soon twist around each other under the mutual induction. The necks, which are physically connected with the head, will also be stretched and twisted as the head experiences the fast developing instability. This evolution will produce lots of small slender vortices and hence quickly yields a new kind of structure, which will be illustrated in the next section.

In addition, many inclined slender streamwise vortices can be observed in figure 10(*a*), which primarily come from the splitting of legs of the hairpin vortices. As the flow goes downstream, the vortices attain even more-slender bodies while their population increases. Some of them come from the stretching of the existing larger vortices while the others are newly generated by the interaction between the main shear and the existing vortices. The striking conclusion is that the slender quasi-streamwise vortices increasingly dominate the transversal middle zone of the mixing layer after the breakup of hairpin legs. We can get a integral view of this from the global picture in figure 5(*b,c*). This phenomenon, though first shown in this paper, has been reported earlier by Rossmann *et al.* (2002) in the experimental investigation of the mixing layer at $M_c = 1.7$. The dominance of the slender quasi-streamwise vortices is expected to contribute significantly to the mixing of the fluid from both sides of the mixing layer.

3.4. *The evolution of the flower structure*

The necklaces have the capacity to sustain themselves with intense vorticity after their formation. Figure 11(*a*) shows the vortex structures of the mixing layer in the streamwise domain [92, 115]. It can be seen that many slender vortices are encircled by the necklaces now. Some of the slender vortices are lifted up from the middle zone of the mixing layer by the induction of the necklaces, while most of them have evolved from the head and the necks following the head instability. Figure 11(*b*) gives the field of the spanwise vorticity on the slice cutting though the middle of the necklaces (refer to figure 11*a*). We can see that the upper red point (near $x = 95$ now) has risen up even more (refer to figure 10*b* for the previous position), which is caused by the continuous self-induction of the necklaces. From figure 11(*a*), we can see that those necklaces still keep their shape basically unchanged. They now look like ribbons tying up the small vortices encircled by them. The entire structures,

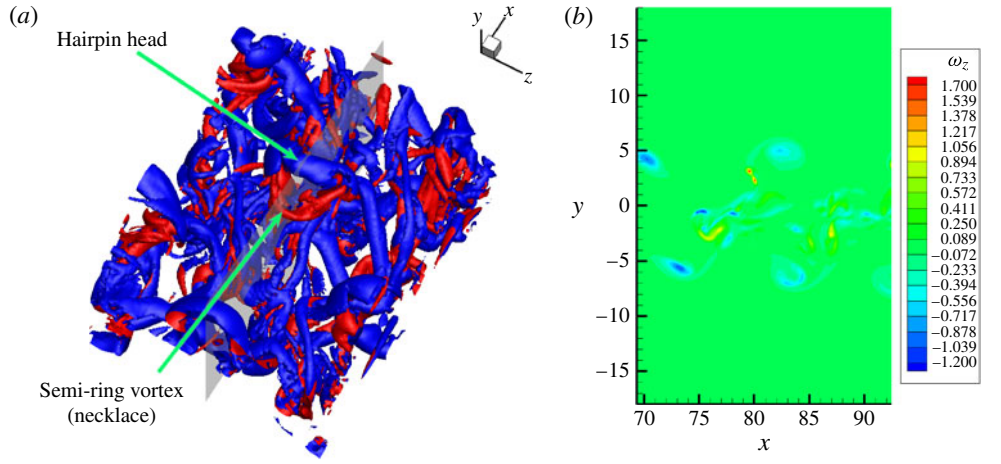

FIGURE 10. (*a*) The vortex structures of the mixing layer in the streamwise domain [69, 93]. Vortices of positive spanwise vorticity are rendered in red, negative in blue. A two-dimensional slice is shown cutting through the head of the hairpin vortex. (*b*) The instantaneous field of the spanwise vorticity on the slice denoted in (*a*). Two red points with strong positive vorticity denote the semi-rings illustrated in (*a*).

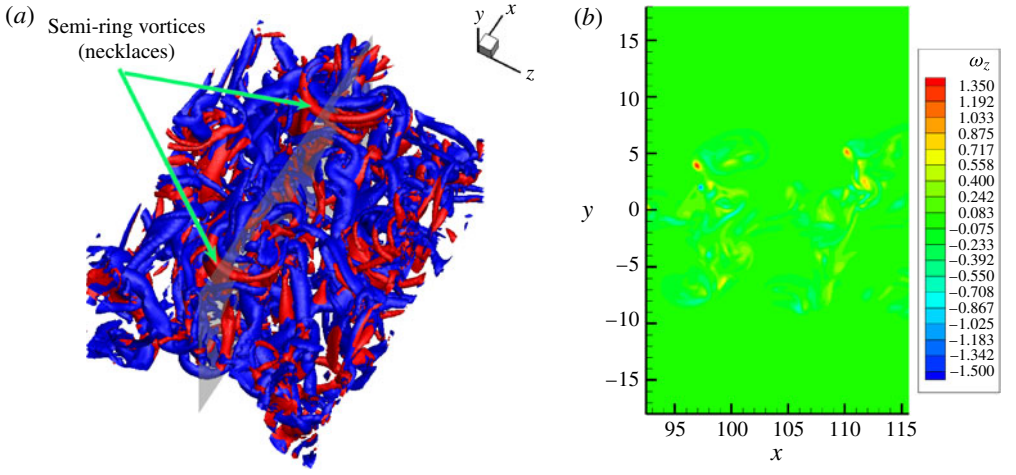

FIGURE 11. (*a*) The vortex structures in the streamwise domain [92, 115]. Vortices of positive spanwise vorticity are rendered in red, negative in blue. The semi-ring vortices together with the slender vortices they embrace form the 'flower' structure. A two-dimensional slice is shown cutting through the middle of the semi-ring vortices. (*b*) The instantaneous field of the spanwise vorticity on the slice denoted in (*a*).

including the necklaces and the encircled small vortices, actually resemble a bundle of flowers. Therefore, we refer to this as a flower structure. For a global view of the flower structures, refer to figure 5. At this stage, the necklaces basically do not interact with other vortices. The relatively independent evolution and the intense vorticity make them attain long lifespans.

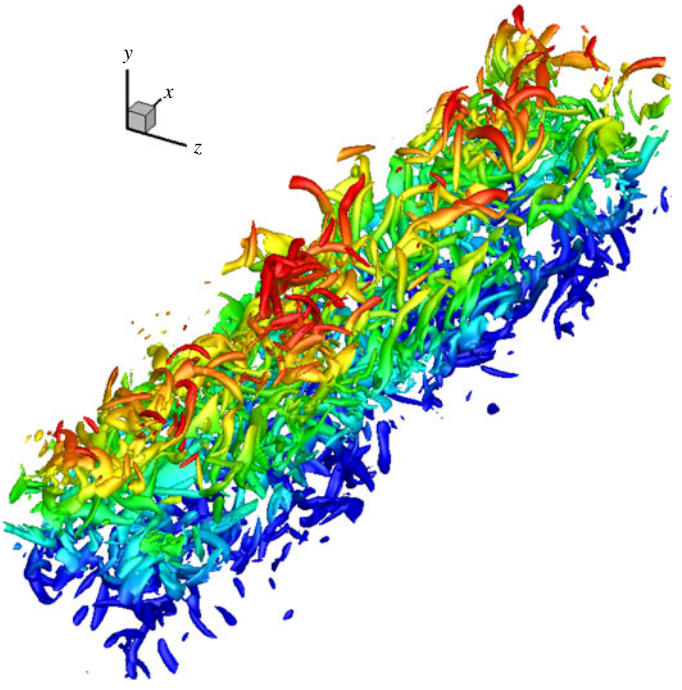

FIGURE 12. Vortex structures in the fully developed turbulence region in the streamwise domain [493, 580]. The vortices are shown using the iso-surfaces of swirl strength with a value of 0.006. The colour changes across the mixing layer from blue to red as y increases.

3.5. *Vortex structures in the self-similar turbulence*

The mixing layer starts to settle down to the fully developed turbulence after the breakup of flower structures. The computed Reynolds stresses data indicate that the flow establishes its self-similar state only when the streamwise distance is beyond 400. Vortex structures in the self-similar region are shown in figure 12. Swirl strength with a value of 0.006 is adopted to fully visualize the small vortices in this region. The colour is rendered from blue to red across the mixing layer for a clear picture of the vertical positions of these vortices. We can see clearly that the middle zone of the mixing layer is still dominated by slender quasi-streamwise vortices. They are much weaker than those appearing in the transition region because most of them will disappear if the swirl strength is tuned up to 0.025, which is the value used for the visualizations in all other regions. Some smaller vortices with random directions can also be identified in the middle zone. The red vortices in the upper layer and the blue ones in the lower layer are mainly the residuals of the flower structures. The vortices in the lower layer seem more abundant and disorganized, which is due to the more compact distribution and the earlier breakup of the vortex structures in the lower layer (see the discussions in § 3.2). Generally, in the self-similar region, all the structures are highly three-dimensional; no organized large-scale two-dimensional structures are observed. This is consistent with previous experimental reports (e.g. Clemens & Mungal 1992; Rossmann *et al.* 2002).

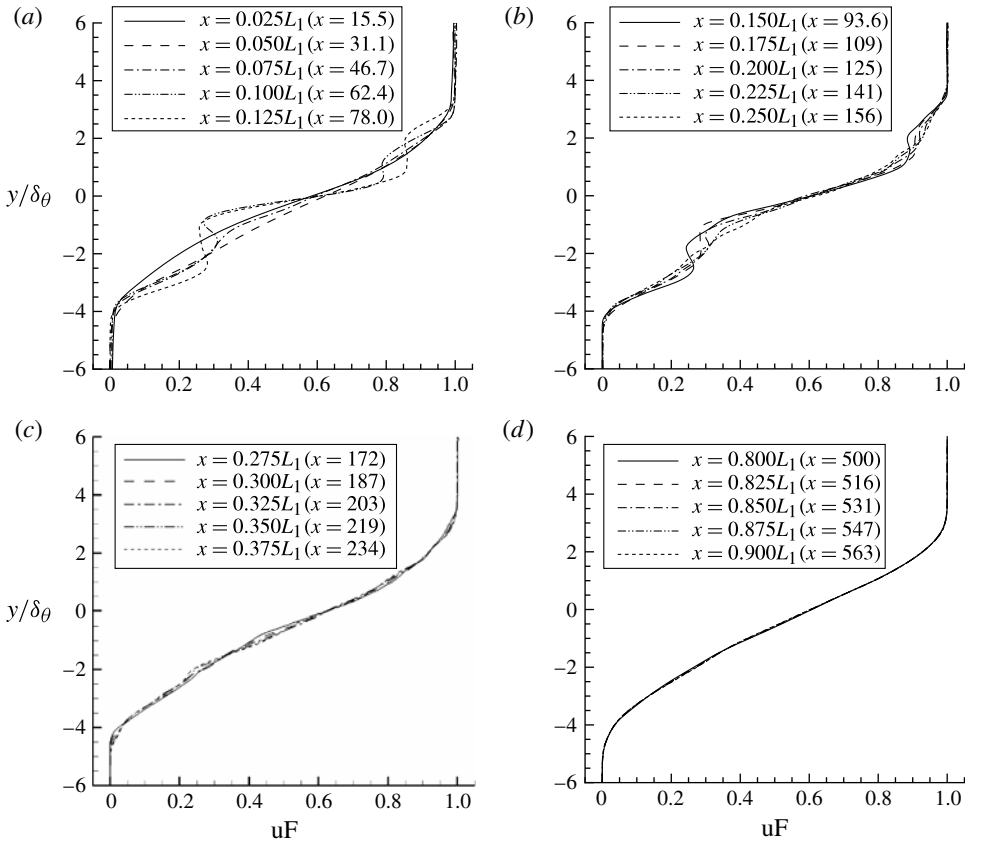

FIGURE 13. Profiles of the mean streamwise velocity across the mixing layer, where uF denotes $(\tilde{u} - U_2)/\Delta U$ (note $\Delta U = (U_1 - U_2)$); (*a–d*) show the profiles at different increasing streamwise positions from the inlet to the fully developed self-similar turbulence region. The apparent distortions of the profiles in (*a,b*) are found to have close connections with the vortex structures in the flow.

4. The evolution of the mean properties

4.1. *The distortion of the mean streamwise velocity profile across the shear layer*

Recently, Watanabe & Mungal (2005) have shown experimentally that the streamwise velocity profile across the shear layer had triple inflection points in a forced compressible mixing layer of $M_c = 0.62$ (see figure 18*a* in their paper). They also reported that the triple inflection points appeared to enhance shear-layer instability, leading to a mixing enhancement. However, the reason for the appearance of inflection points was not discussed in any detail. In our simulation, we also find that the transverse profile of the mean streamwise velocity changes quickly from the typical profile with one inflection point to a shape with triple inflection points. The triple-inflection profile evolves, then is distorted and becomes a quintuple-inflection profile not very far from the inlet (see figure 13*a*). We also refer to the quintuple-inflection profile as a double-S-shaped profile since the new inflection point in the middle of either side makes the local curve look like an 'S'. To the best of our knowledge, S-shaped profiles were first reported by Nygaard & Glezer (1991) and followed by Foss

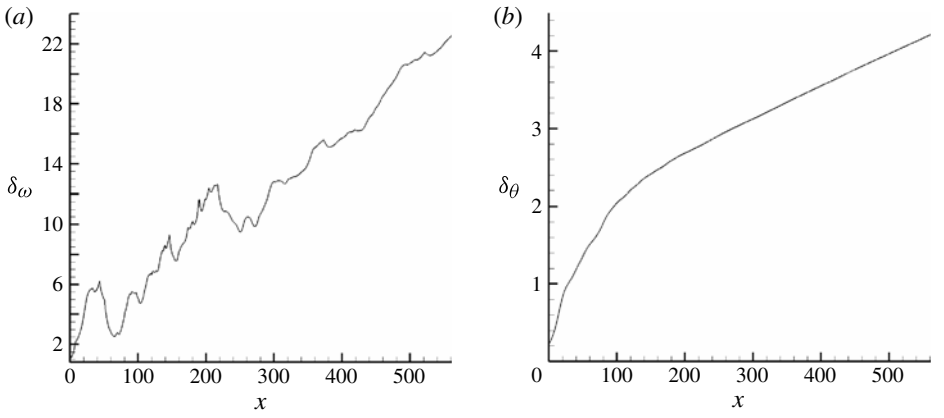

FIGURE 14. (*a*) The evolution of the vorticity thickness of the mixing layer, defined by $\delta_\omega = \Delta U/|\mathrm{d}\tilde{u}/\mathrm{d}y|_{max}$. (*b*) The evolution of the momentum thickness of the mixing layer, defined by $\delta_\theta = (1/\rho_1 \Delta U^2) \int_{-L_y/2}^{L_y/2} \bar{\rho}(U_1 - \tilde{u})(\tilde{u} - U_2)\,\mathrm{d}y$.

& Zaman (1999), both based on their experimental studies of incompressible mixing layers. Moreover, Nygaard & Glezer (1991) noted that the distortion was accompanied by the onset of streamwise vortices.

It would be easier to understand the mechanism of the shape change of the profile with the help of visualization. At the very beginning of the development of the mixing layer, the profile actually keeps its initial form. This is because no vortices have rolled up and the influence of the regular periodic disturbances on the profile is almost totally cancelled after being averaged in both the temporal and spanwise directions. Then, Λ-vortices roll up and start to dominate the flow. The oblique legs of Λ-vortices develop very quickly. They form completely and reach their maximum radius at a short distance from about $x = 10$ to $x = 40$ (see figures 6*a,b* and 7*a*). As the vorticity in the original thin layer is collected into the vortices with cylindrical shape, the roll-up of Λ-vortices yields a rapid increase of the thickness of the mixing layer. From figure 14(*a,b*), the increase can be seen clearly in both the vorticity thickness and the momentum thickness of the mixing layer in the early spatial span. Note that the rapid increase of the vorticity thickness of the mixing layer actually indicates the decrease of the main shear rate, which means that the velocity gradient becomes smaller. From figure 13(*a*) it can be seen that the velocity gradient of the middle part of the profile of $x = 31.1$ does become smaller than that of the profile of $x = 15.5$. It is also worth noting that these two profiles almost collapse onto each other at both ends.

Geometrically speaking, if one smooth curve is close to a one-inflection curve at the two ends but with a less steep middle part, it will produce at least one additional inflection point on each side of the curve to maintain its smoothness. Here, the reader may be also wondering why the ends of the two profiles almost coincide with each other during the vortex roll-up. This issue would be clearer if one considered that the influences of the flow structures are confined in the downstream Mach cone in the supersonic flow and cannot reach the transversal sides instantly. Now, we have fully understood why the profile of $x = 31.1$ has become slightly triple inflectional (see figure 13*a*). Actually, the triple-inflection profiles found in Watanabe & Mungal (2005) had basically the same shape as the profile of $x = 31.1$ in this case. The mechanism of the formation of this kind of shape is also essentially similar since they claimed

that there was a pair of counter-rotating streamwise vortices existing even in the later stages of the flow. However, the triple-inflection profile in the current simulation does not survive for as long a time as that in the experiment of Watanabe & Mungal (2005), which is because in our case the flow structures are still evolving vigorously.

After the roll-up process, legs of Λ-vortices start to flatten under the action of the main shear. The flattened legs, in turn, help make the main shear layer much thinner and stronger by intensifying the vorticity during the flattening process. As mentioned in § 3.2, the legs will experience core dynamic instability. The instability makes the flatten legs and the main shear layer even more intense by accumulating the vorticity in the peripheries of the legs. As a result, the main shear becomes extraordinarily strong in this stage of the development. The strengthening of the main shear can be reflected in the plot of the vorticity thickness versus the streamwise position (figure 14*a*), in which a sudden decrease of the vorticity thickness in the spatial interval [40, 80] can be seen clearly. The decrease indeed corresponds to the increase of the main shear because the vorticity thickness is inversely proportional to the maximum shear rate of the mixing layer ($\delta_\omega = \Delta U/|\mathrm{d}\tilde{u}/\mathrm{d}y|_{max}$). We also notice that the momentum thickness does not reveal this dramatic main shear strengthening trend. This is no surprise because the momentum thickness is based on an integration formula and not very sensitive to the rapid change of flow structures.

From figure 13(*a*), we can see that the slope of the middle part of the profile at the location $x = 62.4$ steepens much more in comparison with the single-inflection profile at $x = 15.5$. We can also see that both ends of the middle steep part of the profile at $x = 62.4$ have become S-shaped. Each 'S' has one inflection point in its middle, plus the pre-existent one in the centre and the other two near each end of the entire curve, making the profile at $x = 62.4$ quintuple inflectional. Observing figure 13(*a*) closely, we can see that the profile at $x = 46.7$ has already become quintuple inflectional, though the S-shape is not as profound as that in the profile at $x = 62.4$. This is because the vortical legs just start to flatten at the location of $x = 46.7$. From the profile at $x = 62.4$, we can see clearly that the 'S' on both sides of the profile gives negative velocity gradient. It would be natural for us to relate this phenomenon to hairpin vortices since both the heads and necks of hairpin vortices pump the flow against the main flow.

To make this clear we present some quantitative data on the transversal positions of hairpin vortices. Going back to figure 8(*b*), we can see that the vortex centres of the hairpin heads on the upper and lower sides are located at around $y = 4$ and $y = -5$ respectively (the streamwise position of the considered heads is roughly between $x = 55$ and $x = 62$). The head vortices induce the surrounding fluid to rotate around them and thus change the flow directions in the local reference frame. This effect is reflected as an inflection point on each side of the mean velocity profile. From careful observation of the profile of $x = 62.4$ in figure 13(*a*), we can see that the highest inflection point, between the upper S and the upper end of the profile, is located at around $y/\delta_\theta = 2.3$. The inflection point near the lower end is located at around $y/\delta_\theta = -3$. Since $\delta_\theta \sim 1.54$ at this streamwise position (see figure 14*b*), the actual transversal positions of the two inflection points can be easily obtained as $y = 3.5$ and $y = -4.6$ respectively. These two points are comparable with the positions of the corresponding head vortices, indicating that the head vortices do affect the mean profile. The energetic necks of the hairpin vortices on both sides pump the flow against the main flow and also outside of the mixing layer. The direct consequence of this action is to decrease or even invert the velocity gradient across that transversal span. The two S-shapes in the profile are produced in this way. As the flow proceeds,

the positions of the head vortices continue to rise away from the middle of the mixing layer. This will cause the inflection points near the two ends of the profile to attain even higher positions, which can be clearly seen from the profile at $x = 78.0$.

The S-shaped velocity profile starts to abate quickly after $x = 78.0$ (see figure 13*a,b*). This is caused by the behaviour of the hairpin vortices, which become unstable and evolve into flower structures in the downstream flow region. The flower structures are composed of small slender vortices and do not have the capacity to induce strong pump flow that the former hairpin vortices did. From figure 13(*b*) we can see that the S-shape has almost disappeared at the streamwise position $x = 141$, where the flower structures start to decay rapidly (see the global view in figure 5*a*). From that position on, the velocity profile starts recovering its single-inflection form. We notice that there are still some slight irregular undulations on each side of the profiles from $x = 172$ to $x = 234$ (see figure 13*c*). It is believed these are caused by the nearly chaotic movements of small vortices in the later transition stages. The velocity profile recovers the single-inflection shape far downstream where the flow has finally evolved into its self-similar turbulent state (see figure 13*d*).

4.2. *The growth rate in the transition region*

Watanabe & Mungal (2005) showed experimentally that their mixing enhancement technique increased shear-layer growth rate by ~50 % at $M_c = 0.62$, and the enhanced rate stayed almost constant in the streamwise direction. Their results might not be so conclusive if we consider that all previous studies have shown that it is extremely hard to increase the growth rate in the late self-similar stage of mixing layer flow. Our simulation results support this generally recognized view. From figure 14(*a,b*), we can see that the growth rates of both vorticity thickness and momentum thickness in the region of $x > 300$ have lower constant values than in $x < 300$. This indicates that the higher growth rates are only achieved in the stages of linear instability and nonlinear transition. Papamoschou & Roshko (1988) presented a criterion to estimate the distance needed for mixing layers to reach their fully developed states, which is $x_{eff}/\theta_1 > 500$, where x_{eff} is an effective length with the definition $x_{eff} = x(1-U_2/U_1)$, in which U_2 and U_1 are the velocities on the low-speed and high-speed sides respectively, and θ_1 is the momentum thickness of the boundary layer in the high-speed side. In our case, the total length of the computational box is ~625 (non-dimensionalized by initial vorticity thickness), and the initial momentum thickness is around 0.2. Assuming the momentum thickness on the high-speed boundary layer side is around half of the momentum thickness of the initial mixing layer, we obtain $x_{eff}/\theta_1 \approx 3125$, which apparently satisfies the criterion. From the curves of both the momentum and vorticity thickness and also the evolution of the flow structures we know that the fully developed state of the flow roughly starts at $x = 300$, which gives $x_{eff}/\theta_1 \approx 1500$. The settling down of the profiles of Reynolds stresses needs an even longer distance, which is around $x = 400$, making $x_{eff}/\theta_1 \approx 2000$. This suggests that the distance needed for a forced mixing layer to reach the fully developed state might be much longer compared with unforced one (which is $x_{eff}/\theta_1 > 500$ as aforementioned).

In the experiments performed by Watanabe & Mungal (2005), we can see that the length of the test tunnel is 220 mm; the momentum thickness of the high-speed boundary layer is 0.12 mm; the velocity ratio is 0.318. These data yield $x_{eff}/\theta_1 \approx 1250$. We should also notice that the thicknesses of the triangular devices mounted on the splitter are at least twice the momentum thickness of the high-speed boundary layer, which would thicken the initial momentum thickness and give an even smaller ratio of x_{eff}/θ_1, probably less than 600. This means that the tunnel length in the experiments

of Watanabe & Mungal (2005) probably was not long enough for the flow to enter its self-similar state. Thus, all the data they obtained might actually indicate that the forced compressible mixing layer could attain a larger growth rate in the nonlinear transition process, which is consistent with our simulation results.

Our simulation also confirmed the commonly recognized view that the mixing layer will finally reach the fully developed state with a constant growth rate and it is hard to enhance this growth rate by adding the disturbance upstream (Townsend 1976, p. 196). However, this does not mean that a disturbance added upstream has virtually no impact on the evolution of the flow. The high growth rate induced by the disturbance in the transition region can increase the thickness of the mixing layer significantly, though the transition process cannot be sustained for a very long period of time. From the momentum thickness curve shown in figure 14(*b*), we can see that the average growth rate from $x = 0$ to $x = 100$ is roughly four times that in the self-similar turbulence region. The tremendous growth rate in the early stages is evidently caused by the vigorous evolution of large structures, including the roll-up of the Λ-vortex and the formation of the hairpin vortex. The high growth rate makes it possible for the mixing layer to attain a large thickness in a shorter distance. This has important practical meaning in the application of supersonic combustion ramjets.

It is noted that the higher growth rate in the early stages has been reported by Liou, Lien & Hwang (1995) through two-dimensional simulations of turbulent free shear layers. They stated that the growth rate of supersonic/supersonic free shear layers increased markedly when the forced layers move up and down with time instead of forming vortex roll-up and pairing. They did not see the recovery of the growth rate in their simulations. The reason might be either that the computational domain was not adequately long, or that the two-dimensional simulations inherently have no capacity to resolve the fully developed turbulence in a physically sound way.

5. The evolution of the Reynolds stresses

The Reynolds stresses in the mixing layer are found to be closely associated with the flow structures. Figure 15 shows the distribution of streamwise Reynolds stress $\bar{\rho}\widetilde{u''u''}/\rho_1\Delta U^2$ at different streamwise positions. (Note that , for convenience, the positions are indicated using fractions of the total length in the streamwise direction. The total length is denoted by L_1. For the exact values of those positions, refer to figure 13.) It can be seen from figure 15(*a*) that the magnitude of $\bar{\rho}\widetilde{u''u''}/\rho_1\Delta U^2$ is relatively high at the positions not far from the inlet where the large structures dominate the flow. The peak value at $x = 0.1L_1$ is about six times that in the self-similar domain (see figure 15*d*). It is interesting to point out that a double-peak profile appears at around $x = 0.075L_1$ and persists at $x = 0.1L_1$. Similar phenomena have been observed by Wygnanski, Oster & Fiedler (1979) and Oster & Wygnanski (1982) in experiments on incompressible shear flow. They conjectured that this kind of phenomenon was caused by a large vortex with violent peripheries but an inactive centre. Here, based on the clear visualizations of the flow structures presented in the above sections, we can relate the double-peak profile directly to the rise of the head of the hairpin vortex on both sides, which instantly induces strong pump flow against the main flow (see figures 7*a* and 8*a*). We can also see that the peak of $\bar{\rho}\widetilde{u''u''}/\rho_1\Delta U^2$ on the lower side is obviously higher than that on the upper side. This is due to the fact that the hairpin head on the lower side rises up earlier and becomes relatively stronger in that streamwise area. Careful observation shows that, at $x = 0.075L_1$ and $x = 0.1L_1$,

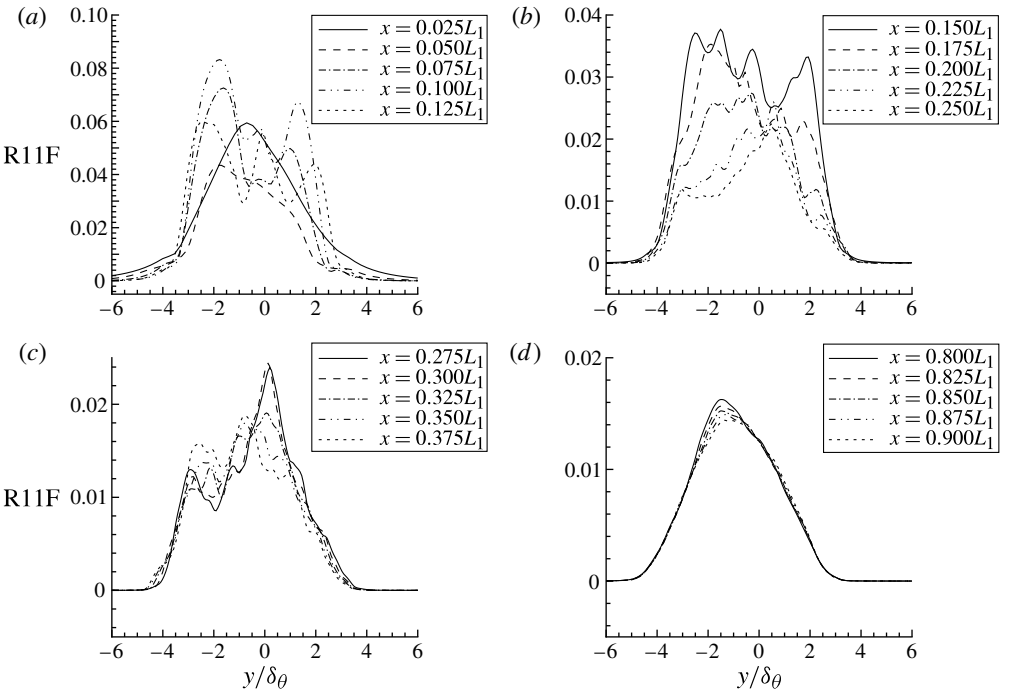

FIGURE 15. The profiles of the streamwise Reynolds stress across the mixing layer, where R11F denotes $\widetilde{\bar{\rho}u''u''}/\rho_1\Delta U^2$; (*a–d*) show the profiles at different streamwise positions from the inlet to the fully developed self-similar turbulence region. The different peak properties of the profiles in (*a,b,c*) are found to have close connections with the vortex structures in the flow.

the peaks are basically in the same transversal areas as the S-shaped curves in the mean streamwise velocity profiles. This confirms the connection between the double peaks and the behaviour of the hairpin vortex.

As the flow goes downstream, the double peaks evolve into triple peaks at $x = 0.125L_1$ (see figure 15*a*). To understand this, we recall the evolution of the structures in the flow. The reason is twofold. First, the two peaks attenuate after the instability of the hairpin vortex. Second, the newly generated quasi-streamwise vortices in the middle zone of the mixing layer still have a strong ability to induce fluid motion around them. The combination of these two factors makes the peak in the middle of the profile appear at around $x = 0.125L_1$. After $x = 0.125L_1$, many small vortices are produced in the middle of the mixing layer. The pronounced peaks in the Reynolds stress profile are smeared out since those small vortices undergo viscous dissipation as the flow continues. One can see multi-peaks with smaller amplitude appearing at further downstream positions in figure 15(*b*). From $x = 0.15L_1$ to $x = 0.3L_1$ in figure 15(*b,c*), it can be seen that the magnitude on the lower side decreases significantly while that on the upper side still keeps a high value. This is because the flower structure on the upper side can survive a relatively long distance (for clarity, refer to figure 9 at that streamwise span). The profile with a single peak is established as the flow reaches its self-similar state at the very late stages (see figure 15*d*).

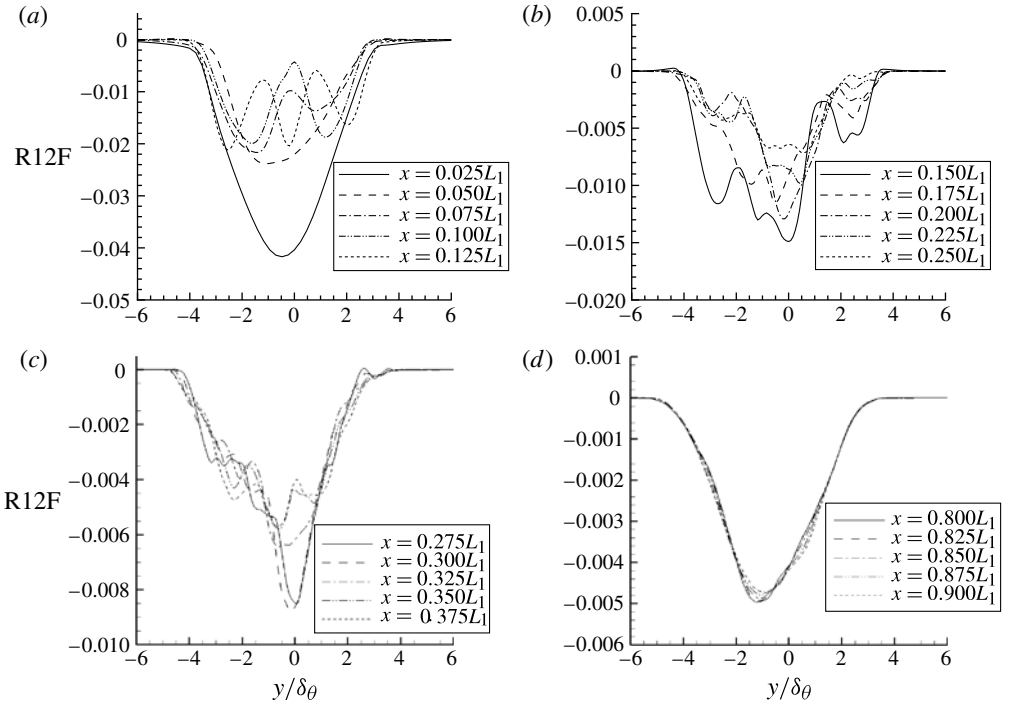

FIGURE 16. Profiles of the Reynolds shear stress across the mixing layer, where R12F denotes $\bar{\rho}\widetilde{u''v''}/\rho_1\Delta U^2$; (*a–d*) show the profiles at different streamwise positions from the inlet to the fully developed self-similar turbulence region.

The spatial evolution of $\bar{\rho}\widetilde{u''v''}/\rho_1\Delta U^2$, $\bar{\rho}\widetilde{v''v''}/\rho_1\Delta U^2$ and $\bar{\rho}\widetilde{w''w''}/\rho_1\Delta U^2$ is displayed in figures 16, 17 and 18 respectively; $\bar{\rho}\widetilde{u''w''}/\rho_1\Delta U^2$ and $\bar{\rho}\widetilde{v''w''}/\rho_1\Delta U^2$ are not displayed here because they are relatively too small and therefore do not bear any significance. From those figures, we can see that the development of $\bar{\rho}\widetilde{u''v''}/\rho_1\Delta U^2$ and $\bar{\rho}\widetilde{v''v''}/\rho_1\Delta U^2$ is similar to that of $\bar{\rho}\widetilde{u''u''}/\rho_1\Delta U^2$. This is easy to understand if the Reynolds stress transport mechanisms are considered. Though the details of this topic are beyond the scope of the current paper, we point out that $\bar{\rho}\widetilde{v''v''}/\rho_1\Delta U^2$ dominates the production terms of $\bar{\rho}\widetilde{u''v''}/\rho_1\Delta U^2$ while $\bar{\rho}\widetilde{u''v''}/\rho_1\Delta U^2$ is the only Reynolds stress that appears in the production terms of $\bar{\rho}\widetilde{u''u''}/\rho_1\Delta U^2$. The spanwise Reynolds stress term $\bar{\rho}\widetilde{w''w''}/\rho_1\Delta U^2$ does not have as close relations with other Reynolds stresses. This is why the double or triple peaks in $\bar{\rho}\widetilde{w''w''}/\rho_1\Delta U^2$ are not as pronounced as those in $\bar{\rho}\widetilde{u''u''}/\rho_1\Delta U^2$, $\bar{\rho}\widetilde{u''v''}/\rho_1\Delta U^2$ and $\bar{\rho}\widetilde{v''v''}/\rho_1\Delta U^2$ (compare figure 18*a* to figures 15*a*, 16*a* and 17*a*).

Moreover, we can see that the magnitudes of the three normal Reynolds stresses in the self-similar region have the relation: $\bar{\rho}\widetilde{u''u''}/\rho_1\Delta U^2 > \bar{\rho}\widetilde{w''w''}/\rho_1\Delta U^2 > \bar{\rho}\widetilde{v''v''}/\rho_1\Delta U^2$, representing that the turbulence in the mixing layer possesses the characteristics of strong three-dimensionality. This is consistent with the findings of Gruber *et al.* (1993) (experimentally) and Pantano & Sarkar (2002) (numerically).

Comparisons between our results and some experimental results are made in figure 19. We can see that only $\bar{\rho}\widetilde{v''v''}/\rho_1\Delta U^2$ of the present simulation agrees very

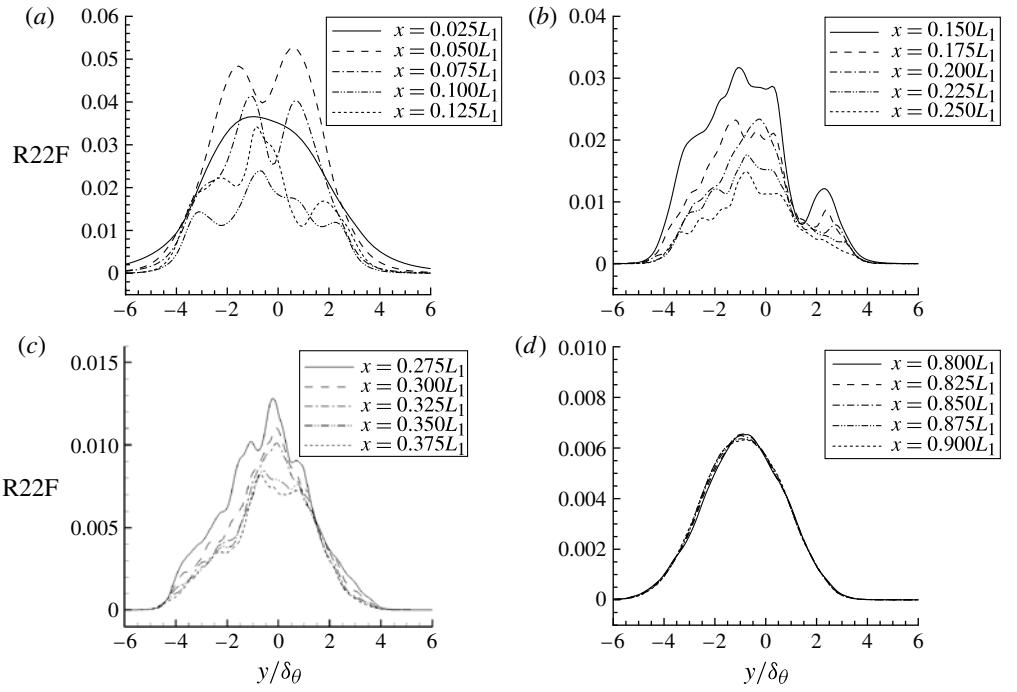

FIGURE 17. Profiles of the transversal Reynolds stress across the mixing layer, where R22F denotes $\bar{\rho}\widetilde{v''v''}/\rho_1\Delta U^2$; (*a–d*) show the profiles at different streamwise positions from the inlet to the fully developed self-similar turbulence region.

well with the experimental results for $M_c = 0.69$ from Goebel & Dutton (1991). Other Reynolds stresses are apparently smaller than those from Goebel & Dutton (1991) and Gruber *et al.* (1993). However, we can also see that $\bar{\rho}\widetilde{u''u''}/\rho_1\Delta U^2$, $\bar{\rho}\widetilde{v''v''}/\rho_1\Delta U^2$ and $\bar{\rho}\widetilde{u''v''}/\rho_1\Delta U^2$ are close to, though still slightly lower than, the experimental results obtained by Elliott & Samimy (1990) at $M_c = 0.86$. The low value of the Reynolds number adopted in the present simulation could be a possible reason for the relatively small Reynolds stresses. Besides, as stated in the Introduction section, there are still some controversies regarding $\bar{\rho}\widetilde{u''u''}/\rho_1\Delta U^2$ and $\bar{\rho}\widetilde{w''w''}/\rho_1\Delta U^2$ in previous investigations. We conjecture that these two Reynolds stresses can be influenced easily by the particular evolution procedure before the flow enters the self-similar state. This speculation could explain why controversies regarding $\bar{\rho}\widetilde{u''u''}/\rho_1\Delta U^2$ and $\bar{\rho}\widetilde{w''w''}/\rho_1\Delta U^2$ occur both experimentally and numerically. To explore the intrinsic reason behind this phenomenon, carefully designed numerical or experimental investigations are needed. Though there are some discrepancies in the absolute magnitudes of the Reynolds stresses, very good agreement on the Reynolds stress anisotropy is found between the present simulation and previous investigations. The peak Reynolds stresses ratios, $(\bar{\rho}\widetilde{v''v''}/\bar{\rho}\widetilde{u''u''})^{1/2}$ and $(\bar{\rho}\widetilde{u''v''}/\bar{\rho}\widetilde{u''u''})^{1/2}$, are found to be 0.652, 0.566 respectively. The corresponding data are 0.648, 0.543 in Elliott & Samimy (1990), and 0.673, 0.568 in the numerical work of Pantano & Sarkar (2002). The consistent Reynolds stress anisotropy indicates that the turbulence structure captured in this paper is similar to those in previous investigations. An extensive

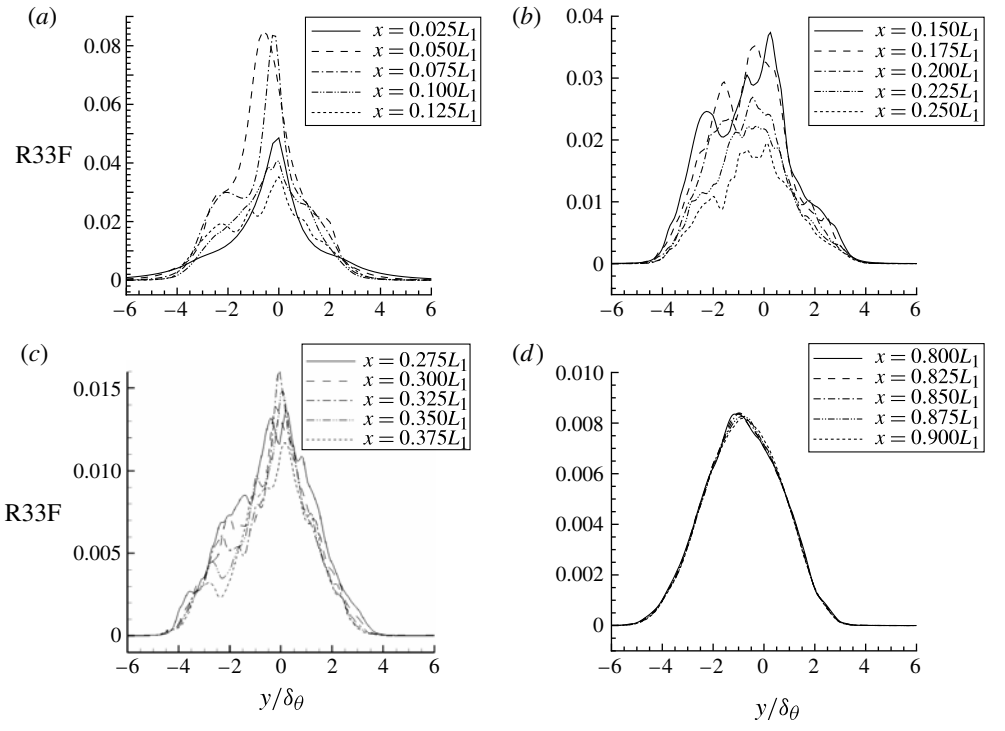

FIGURE 18. Profiles of the spanwise Reynolds stress across the mixing layer, where R33F denotes $\bar{\rho}\widetilde{w''w''}/\rho_1\Delta U^2$; (*a–d*) show the profiles at different streamwise positions from the inlet to the fully developed self-similar turbulence region.

comparison of Reynolds stress anisotropy has been conducted by Barre *et al.* (1997), showing that it is almost constant up to convective Mach number close to unity. The peak Reynolds stress ratios computed from Goebel & Dutton (1991) are different from those consistent data (see figure 6 in Barre *et al.* 1997). This is because their reported $\bar{\rho}\widetilde{u''u''}/\rho_1\Delta U^2$ does not decrease much as M_c increases.

6. Shocklets in the mixing layer

To our best knowledge, shocklets were first captured in the simulations of three-dimensional decaying compressible turbulence performed by Kida & Orszag (1990). The appearance of shocklets in simulations of three-dimensional compressible mixing layers was first reported by Vreman *et al.* (1995). However, until now, there has been no universally accepted criterion for the identification of shocklets. In most numerical applications (e.g. Kourta & Sauvage 2002; Fu & Li 2006), shocklets are visualized in two-dimensional slices, which can only provide limited information on the flow field near the shocklets. In this paper, we will adopt the method employed by Vreman *et al.* (1995) and Freund *et al.* (2000), which visualizes shocklets in three-dimensional space using the iso-surface of negative dilatation. Rankine–Hugoniot jump conditions are checked to make sure the iso-surfaces are actual shocklets. The most important advantage of this method is that it shows straightforwardly three-dimensional shapes of shocklets. In the framework of this three-dimensional visualization, extra information such as vortical structures can easily be furnished to help understand the generation

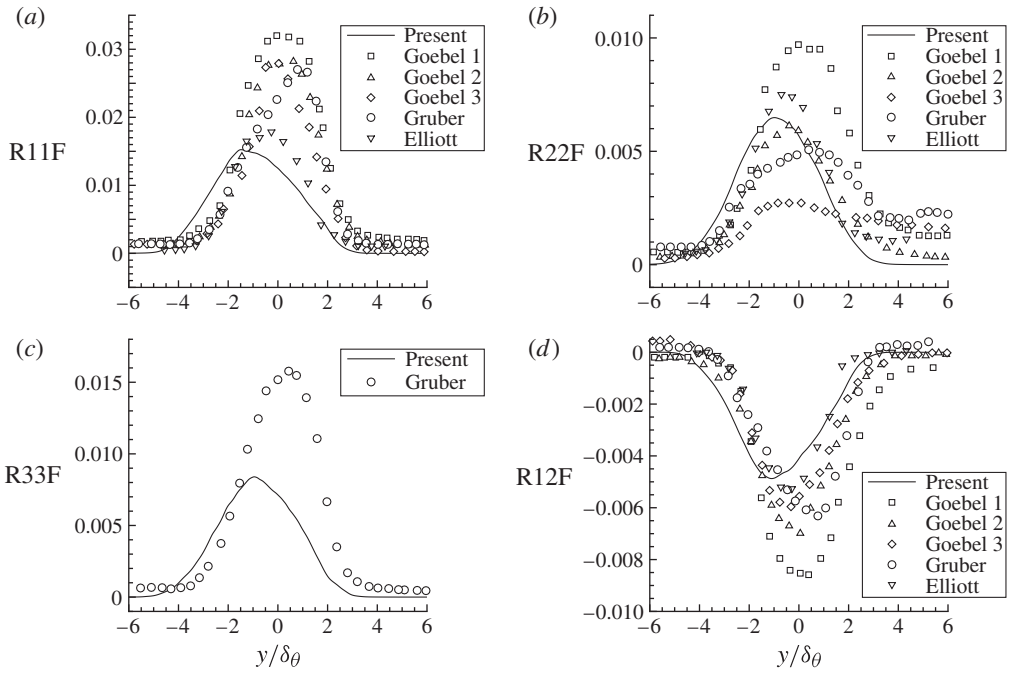

FIGURE 19. Comparisons of the Reynolds stresses in the self-similar region between the present results and some experimental results, where Gruber stands for the results for $M_c = 0.8$ by Gruber *et al.* (1993), Elliott for $M_c = 0.86$ by Elliott & Samimy (1990), and Goebel1, Goebel2 and Goebel3 those by Goebel & Dutton (1991) for $M_c = 0.46$, 0.69, 0.99 respectively. (*a*) Streamwise, (*b*) transverse, (*c*) spanwise, (*d*) shear. Note, Gruber *et al.* (1993) is the only source we can find for R33F ($\widetilde{\bar{\rho}w''w''}/\rho_1\Delta U^2$).

mechanisms of these shocklets. In the following, shocklets will be identified by the iso-surface of $\nabla \cdot \boldsymbol{u} = -0.1$, rendered in red. Generally, shocklets have a finite thickness in viscous flow and in our case the shock thickness is approximately twice the grid size.

Figure 20(*a*) shows the shocklets near a Λ-vortex. Two kinds of shocklets can be identified from this figure. The first kind appears in strips, attaching to the legs of the Λ-vortex. To illustrate their generation mechanism clearly, figure 20(*b*) shows the instantaneous pressure information on a two-dimensional slice cutting through the legs (see figure 20*a*). We can see that the fluid around every leg is rotating due to the induction of the legs. The shocklets are generated instantly when the fluid encounters the relatively high-pressure zone around the leg. Another kind of shocklet is located on the head of the Λ-vortex. It has been captured by Rossmann *et al.* (2002) in their schlieren experiments. They stated that their formation mechanism shows good agreement with the scenario of flow around a bluff body with the vortex protruding to the free stream acting as the bluff body (see figure 21*a*, which is figure 15 in Rossmann *et al.* 2002). Here, in our case, the rotating head of the Λ-vortex improves the formation process by inducing the fluid around the head to attain a higher velocity (see figure 20*d* for a better understanding). So, the mechanism here is twofold, including bluff-body effects and the vortex-head induction. For clarity, a simple diagram is also presented for the mechanism illustrated in this paper (see figure 21*b*). The pronounced difference between the two diagrams in figure 21 is that the shocklets are located at the trailing edge of the large structures in our study

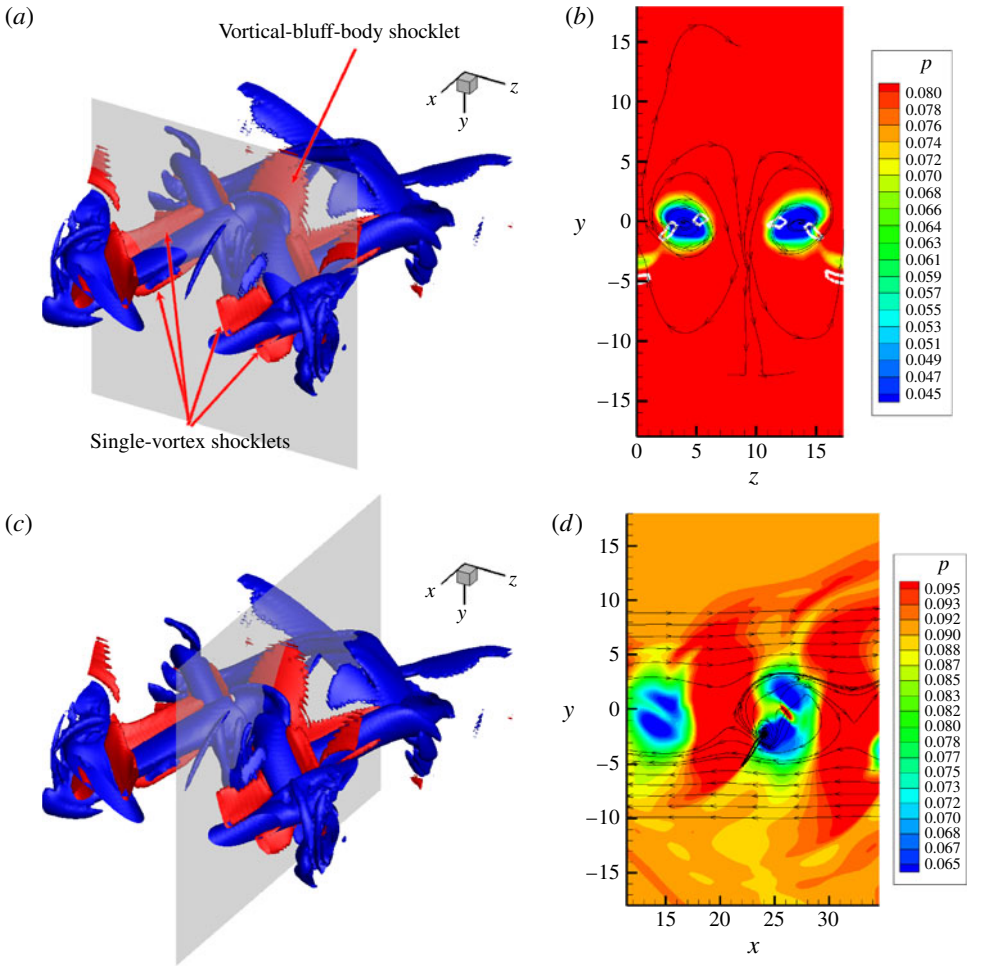

FIGURE 20. (*a*) The shocklet structures in the mixing layer when Λ-vortices dominate the flow. The shocklets are rendered in red. The two-dimensional slice cuts through the legs of a Λ-vortex. (*b*) The pressure field on the two-dimensional slice denoted in (*a*) with the cross-sections of the shocklets shown in white. (*c*) The two-dimensional slice cuts through the head of the Λ-vortex. (*d*) The pressure field on the slice denoted in (*c*) with the cross-sections of the shocklets shown in black. On (*b*) and (*d*), streamlines are shown in the local frame moving with vortex structures.

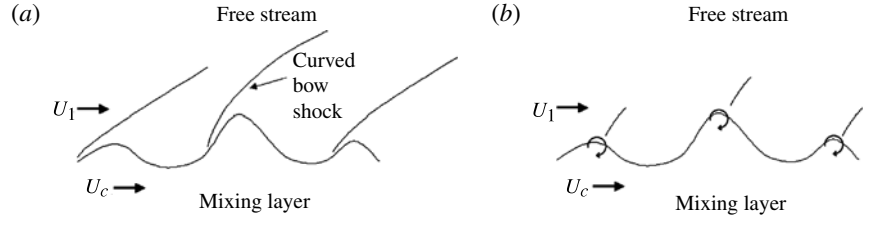

FIGURE 21. (*a*) Schematic diagram of the occurrence of shocklets at $M_c = 1.7$ by Rossmann *et al.* (2002). (*b*) Schematic diagram of the occurrence of shocklets at $M_c = 0.7$ in this paper. The prominent difference is that the vortex induction mechanism is considered in (*b*).

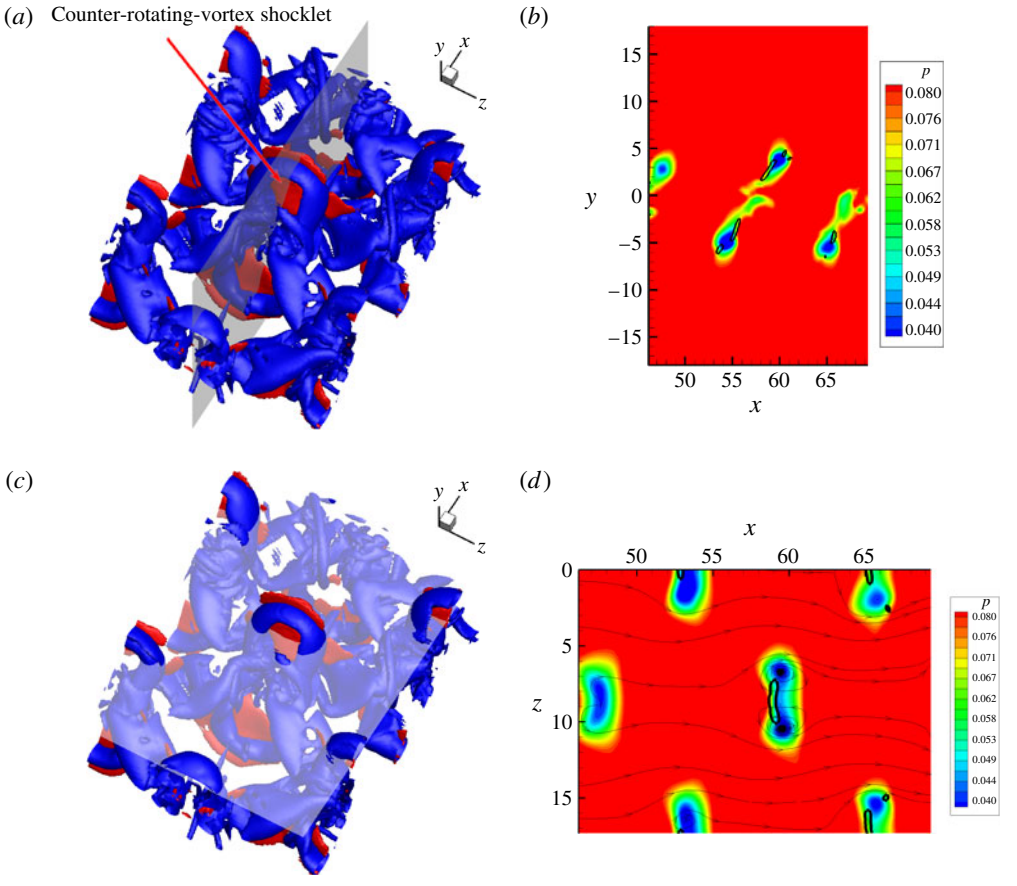

FIGURE 22. (*a*) The shocklet structures in the mixing layer when hairpin vortices dominate the flow. The shocklets are rendered in red. The two-dimensional slice cuts through the head of a hairpin vortex. (*b*) The pressure field on the slice denoted in (*a*) with the cross-sections of the shocklets shown in black. (*c*) The two-dimensional slice cuts through the necks of the hairpin vortex. (*d*) The pressure field on the slice denoted in (*c*) with the cross-sections of the shocklets shown in black. The streamlines are shown in the local frame moving with vortex structures.

while they are attached at the leading edge in the investigation by Rossmann *et al.* (2002). This difference is reasonable if we consider that the convective Mach number ($M_c = 1.7$) in their work is much larger and that larger M_c would give stronger shocklets and move their positions forward. Through the three-dimensional view of figure 20(*a*), we can have a clear look at the shape of this kind of shocklet. They much resemble the peak of a cap with a curved body in the spanwise direction. This is because the spanwise middle section of the vortex head possesses stronger intensity and the stronger intensity can make the fluid around it reach a high relative supersonic velocity sooner. For convenience, the first and second kinds of shocklets will be referred to as single-vortex shocklets and vortical-bluff-body shocklets based on their formation mechanism.

After a hairpin vortex forms, another kind of shocklet appears. Figure 22(*a*) shows a shocklet located between the necks. In order to elucidate the formation mechanism,

the pressure fields on two slices are extracted and displayed in figures 22(*b*) and 22(*d*). From these figures, we can learn that both the head and the necks contribute in the formation process. Most of the contribution comes from the counter-rotating necks since the shocklet fills the entire space between them. This shocklet attains quite a flat body with the middle part bending slightly in the direction of the pump flow between the necks (see figure 22*d*). This kind of shocklet is referred to as a counter-rotating-vortex shocklet according to its generation mechanism. Observing closely, we can also see a small piece of the second kind of shocklet on the hairpin head on figure 22(*a*). Here, the hairpin head is located closer to the free stream. The free stream furnishes a smaller pressure difference across the hairpin head (see the pressure fields around hairpin heads in figures 22*b* and 20*d*). This is believed to be the reason for the shocklet shrinkage. It should also be noted that we do not see first kind of shocklet here. This is understandable, since the hairpin legs are undergoing breakup at this streamwise position. The newly generated small vortices have no capacity of inducing the surrounding fluid to reach a relative supersonic speed.

All the shocklets identified above move along with the vortices that give birth to them as long as those vortices are strong enough to sustain them. No shocklets are found after the head of the hairpin vortex loses its stability and evolves into the flower structure. Generally speaking, the vortical-bluff-body shocklet and single-vortex shocklet are relatively weaker than the counter-rotating-vortex shocklet. In this study, the pressure ratio of the first two kinds of shocklets is around 1.20 while that of the third kind reaches around 1.35. This is not surprising since the collaboration of counter-rotating vortices produces stronger inducing effects. Besides, we notice that Rossmann *et al.* (2002) did not report any shocklets located inside the mixing zone of the mixing layer other than the ones protruding into the free streams. Based on the illustrations above, one can see that the bodies of the single-vortex and counter-rotating-vortex shocklets do not all extend in the spanwise direction. This would smear out the sharp boundaries of the shocklets since the schlieren method integrates through the spanwise direction. Therefore, in order to observe the shocklets in the mixing zone, more advanced devices are needed.

In previous three-dimensional simulations, shocklets were observed at $M_c = 1.2$ (Vreman *et al.* 1995; Kourta & Sauvage 2002; Fu & Li 2006). In particular, Freund *et al.* (2000) reported that they did not observe shocklets until $M_c = 1.54$. However, we captured shocklets at $M_c = 0.7$ in a three-dimensional simulation, which is the lowest convective Mach number reported. There are several possible explanations for this. First, it might be due to the lack of a universal criterion for identifying shocklets. Different criteria would bring different observations. Second, the resolution of simulations depends on the grid spacing and also on the capacity of numerical schemes. In our simulation, the grid spacing probably is the smallest among those reported simulations. Also, the numerical scheme adopted here has better resolution than other commonly used compact schemes. The reader can refer to Zhou *et al.* (2007) for the details of the comparison between those schemes. Third, a relatively larger disturbance is introduced through the inlet in our study, which leads to stronger vortical structures. Based on the mechanisms elaborated above, this factor might contribute greatly to the shocklet formation at convective Mach number as low as $M_c = 0.7$.

7. Concluding remarks

This paper presents a direct numerical simulation of the spatially developing compressible plane mixing layer at $M_c = 0.7$. The mixing layer is forced by a pair of

equal and opposite oblique instability waves and also by relatively weak disturbances from an isentropic vortex model. Flow visualizations show that the flow in early stages is dominated first by Λ structures and then by hairpin vortices. In the present simulation, all the hairpin vortices evolve into newly identified structures, referred to as flower structures, after the hairpin head instability. The new structures are composed of many slender small vortices and look like flower bouquets, with semi-ring vortices as tying ribbons. They are observable until the flow starts to settle down into its self-similar state. In addition, the preponderance of slender quasi-streamwise vortices is observed in the transversal middle of both the transitional region and the self-similar turbulent zone. This phenomenon, though first clearly shown in numerical results of this paper, has been reported earlier by Rossmann *et al.* (2002) in their experimental investigation at $M_c = 1.7$.

Both the evolution of the mean streamwise velocity profile and of the Reynolds stresses is found to be related closely to the behaviours of the large vortex structures. The streamwise velocity profile is found to have triple inflection points not far from the inlet. It evolves quickly into a quintuple-inflection profile after that. It is illustrated that all the distortion of the profile comes from the evolution of the large structures. This was not previously well-explained owing to the restrictions of the experimental devices. In addition, the profiles of all Reynolds stresses are also affected by the vigorous development of vortex structures. Double-peak and triple-peak profiles are observed and explained in the transition region.

Regarding mixing enhancement, it has been becoming a common view that it seems extremely hard, if not impossible, to increase the growth rate in the self-similar turbulence region since in that region 'conditions at the initiation of the flow are highly irrelevant' (Townsend 1976, p. 196). From the simulation, we clearly see that the growth rate in the transition region is much higher (roughly four times) than that in the final self-similar region. This higher growth rate is contributed directly by the energetic evolution of large-scale structures, and intrinsically by the disturbances introduced at the inlet. Recent experiments performed by Watanabe & Mungal (2005) also showed that the growth rate can be enhanced by 50 % by using proper disturbing devices upstream. This demonstrates that the mixing layer thickness can be increased, probably very dramatically, before the flow achieves the final fully developed state. This finding has important practical meaning. Researchers can focus on looking for strategies to increase the thickness of the flow in the transition region and focus less on the slow-growing thickened layer in the self-similar region, where the fluid in the thickened layer can be well mixed at small scales.

Shocklets are observed in the simulation. This is the first three-dimensional simulation that captures the shocklets at this low convective Mach number. The large vortex structures are found to play a significant role in the occurrence of the shocklets. The shocklets are categorized into single-vortex shocklets, vortical-bluff-body shocklets and counter-rotating-vortex shocklets based on their formation mechanisms. No shocklets are found in the fully developed turbulence where the flow is populated by small slender vortices.

Acknowledgements

The computation was supported by Computer Network Information Center, Chinese Academy of Sciences (CNIC, CAS). The authors are grateful for the support of the National Natural Science Foundation of China (Nos. 11072130 and 10932005).

REFERENCES

BARRE, S., BRAUD, P., CHAMBRES, O. & BONNET, J. P. 1997 Influence of inlet pressure conditions on supersonic turbulent mixing layers. *Exp. Therm. Fluid Sci.* **14** (1), 68–74.

BATCHELOR, G. K. 1959 *The Theory of Homogeneous Turbulence*. Cambridge University Press.

BIRCH, S. F. & EGGERS, J. M. 1973 Free turbulent shear flows. *Tech. Rep.* SP-321. NASA.

BOGDANOFF, D. W. 1983 Compressibility effects in turbulent shear layers. *AIAA J.* **21**, 926–927.

BROWN, G. L. & ROSHKO, A. 1974 On density effects and large structure in turbulent mixing layers. *J. Fluid Mech.* **64**, 775–816.

CLEMENS, N. T. & MUNGAL, M. G. 1992 Two- and three-dimensional effects in the supersonic mixing layer. *AIAA J.* **30**, 973–981.

CLEMENS, N. T. & MUNGAL, M. G. 1995 Large-scale structure and entrainment in the supersonic mixing layer. *J. Fluid Mech.* **284**, 171–216.

DAVOUDZADEH, F., MCDONALD, H. & THOMPSON, B. E. 1995 Accuracy evaluation of unsteady cfd numerical schemes by vortex preservation. *Comput. Fluids* **24**, 883–895.

DAY, M. J. & REYNOLDS, W. C. 1998 The structure of the compressible reacting mixing layer: insights from linear stability analysis. *Phys. Fluids* **10** (4), 993–1007.

DIMOTAKIS, P. E. 1991 Turbulent free shear layer mixing and combustion. In *High-speed Flight Propulsion Systems* (ed. S. N. B. Murthy & E. T. Curran), *Progress in Astronautics and Aeronautics*, vol. 137, pp. 265–340. AIAA.

ELLIOTT, G. S. & SAMIMY, M. 1990 Compressibility effects in free shear layers. *Phys. Fluids* A **2**, 1231–1240.

FOSS, J. K. & ZAMAN, K. B. M. Q. 1999 Large- and small- scale vortical motions in a shear layer perturbed by tabs. *J. Fluid Mech.* **382**, 307–329.

FREUND, J. B., LELE, S. K. & MOIN, P. 2000 Compressibility effects in a turbulent annular mixing layer. Part 1. Turbulence and growth rate. *J. Fluid Mech.* **421**, 229–267.

FU, D. X., MA, Y. W. & ZHANG, L. B. 2000 Direct numerical simulation of transition and turbulence in compressible mixing layer. *Sci. China* A **43** (4), 421–429.

FU, S. & LI, Q. B. 2006 Numerical simulation of compressible mixing layers. *Intl J. Heat Fluid Flow* **27**, 895–901.

GOEBEL, S. G. & DUTTON, J. C. 1991 Experimental study of compressible turbulent mixing layers. *AIAA J.* **31**, 538–546.

GRUBER, M. R., MESSERSMITH, N. L. & DUTTON, J. C. 1993 Three-dimensional velocity field in a compressible mixing layer. *AIAA J.* **31**, 2061–2067.

HALL, J. L., DIMOTAKIS, P. E. & ROSEMANN, H. 1993 Experiments in non-reacting compressible shear layers. *AIAA J.* **31**, 2247–2254.

HEISENBERG, W. 1948 Zur statistischen theorie der turbulenz. *Z. Phys.* **124**, 628–657.

JIANG, G. S. & SHU, C. W. 1996 Efficient implementation of weighted eno schemes. *J. Comput. Phys.* **126**, 202–228.

KIDA, S. & ORSZAG, S. A. 1990 Enstrophy budget in decaying compressible turbulence. *J. Sci. Comput.* **5** (1), 1–34.

KOURTA, A. & SAUVAGE, R. 2002 Computation of supersonic mixing layers. *Phys. Fluids* **14** (11), 3790–3797.

LELE, S. 1989 Direct numerical simulation of compressible free shear flows. *AIAA Paper* 1989-0374.

LIEPMANN, H. W. & LAUFER, J. 1947 Investigation of free turbulent mixing. *Tech. Rep.* 1257. NACA.

LIOU, T., LIEN, W. & HWANG, P. 1995 Compressibility effects and mixing enhancement in turbulent free shear flows. *AIAA J.* **33**, 2332–2338.

MOORE, C. J. 1978 The effect of shear layer instability on jet exhaust noise. In *Structure and Mechanisms of Turbulence* (ed. H. Fiedler), *Lecture Notes in Physics*, vol. 76, pp. 254–264. Springer.

MORDUCHOW, M. & LIBBY, P. A. 1949 On a complete solution of the one-dimensional flow equations of a viscous, heat conducting, compressible gas. *J. Aero. Sci.* **16**, 674–684.

MOSER, R. D. & ROGERS, M. M. 1993 The three-dimensional evolution of a plane mixing layer: pairing and transition to turbulence. *J. Fluid Mech.* **247**, 275–320.

NYGAARD, K. J. & GLEZER, A. 1991 Evolution of streamwise vortices and generation of small-scale motion in a plane mixing layer. *J. Fluid Mech.* **231**, 257–301.

OLSEN, M. G. & DUTTON, J. C. 2003 Planar velocity measurements in a weakly compressible mixing layer. *J. Fluid Mech.* **486**, 51–77.

ORTWERTH, P. J. & SHINE, A. 1977 On the scaling of plane turbulent shear layers. *Tech. Rep.* TR-77-118. AFWL.

OSTER, D. & WYGNANSKI, I. 1982 The forced mixing layer between parallel streams. *J. Fluid Mech.* **113**, 91–130.

PANTANO, C. & SARKAR, S. 2002 A study of compressibility effects in the high-speed turbulent shear layer using direct simulation. *J. Fluid Mech.* **451**, 329–371.

PAPAMOSCHOU, D. 1989 Structure of the compressible turbulent shear layer. *AIAA Paper* 1989-0126.

PAPAMOSCHOU, D. 1995 Evidence of shocklets in a counterflow supersonic shear layer. *Phys. Fluids* **7**, 233–235.

PAPAMOSCHOU, D. & ROSHKO, A. 1988 The compressible turbulent shear layer: an experimental study. *J. Fluid Mech.* **197**, 453–477.

PRADEEP, D. S. & HUSSAIN, F. 2000 Core dynamics of a coherent structures: a prototypical physical-space cascade mechanism? In *Turbulence Structure and Vortex Dynamics* (ed. J. C. R. Hunt & J. C. Vassilicos). Cambridge University Press.

ROGERS, M. M. & MOSER, R. D. 1992 The three-dimensional evolution of a plane mixing layer: the Kelvin–Helmholtz rollup. *J. Fluid Mech.* **243**, 183–226.

ROSSMANN, T., MUNGAL, M. G. & HANSON, R. K. 2002 Evolution and growth of large-scale structures in high compressibility mixing layers. *J. Turbul.* **3**, 009.

SAMIMY, M. & ELLIOT, G. S. 1990 Effects of compressibility on the characteristics of free shear layers. *AIAA J.* **28**, 439–445.

SANDHAM, N. D. & REYNOLDS, W. C. 1990 Compressible mixing layer: linear theory and direct simulation. *AIAA J.* **28**, 618–624.

SANDHAM, N. D. & REYNOLDS, W. C. 1991 Three-dimensional simulations of large eddies in the compressible mixing layer. *J. Fluid Mech.* **224**, 133–158.

SCHOPPA, W., HUSSAIN, F. & METCALFE, R. W. 1995 A new mechanism of small-scale transition in a plane mixing layer: core dynamics of spanwise vortices. *J. Fluid Mech.* **298**, 23–80.

SPITERI, R. J. & RUUTH, S. J. 2003 Non-linear evolution using optimal fourth-order strong-stability-preserving Runge–Kutta methods. *Math. Comput. Simul.* **62**, 125–135.

STEGER, J. L. & WARMING, R. F. 1981 Flux vector splitting of the inviscid gasdynamic equations with application to finite difference methods. *J. Comput. Phys.* **40**, 263–293.

THOMPSON, K. W. 1987 Time dependent boundary conditions for hyperbolic systems. *J. Comput. Phys.* **68**, 1–24.

TOWNSEND, A. A. 1976 *The Structure of Turbulent Shear Flows*, 2nd edn. Cambridge University Press.

URBAN, W. D. & MUNGAL, M. G. 2001 Planar velocity measurements in compressible mixing layers. *J. Fluid Mech.* **431**, 189–222.

VREMAN, B., KUERTEN, H. & GEURTS, B. 1995 Shocks in direct numerical simulation of the confined three-dimensional mixing layer. *Phys. Fluids* **7** (9), 2105–2107.

WATANABE, S. & MUNGAL, M. G. 2005 Velocity fields in mixing-enhanced compressible shear layers. *J. Fluid Mech.* **522**, 141–177.

WU, X. & MOIN, P. 2009 Direct numerical simulation of turbulence in a nominally zero-pressure-gradient flat-plate boundary layer. *J. Fluid Mech.* **630**, 5–41.

WYGNANSKI, I., OSTER, D. & FIEDLER, H. 1979 A forced, plane, turbulent mixing-layer: a challenge for the predictor. In *Turbulent Shear Flows* (ed. L. J. S. Bradbury, F. Durst, B. E. Launder, F. W. Schmidt & J. H. Whitelaw). Springer.

ZHOU, J., ADRIAN, R. J. & BALACHANDAR, S. 1999 Mechanisms for generating coherent packets of hairpin vortices in channel flow. *J. Fluid Mech.* **387**, 353–396.

ZHOU, Q., YAO, Z. H., HE, F. & SHEN, M. Y. 2007 A new family of high-order compact upwind difference schemes with good spectral resolution. *J. Comput. Phys.* **227** (2), 1306–1339.